Wideband Signal Generation at Millimeter-Wave and Sub-THz Frequencies

by

Zi Jun Su

A thesis
presented to the University of Waterloo
in fulfillment of the
thesis requirement for the degree of
Master of Applied Science
in
Electrical and Computer Engineering

Waterloo, Ontario, Canada, 2025

© Zi Jun Su 2025

Author's Declaration

This thesis consists of material all of which I authored or co-authored: see Statement of Contributions included in the thesis. This is a true copy of the thesis, including any required final revisions, as accepted by my examiners.

I understand that my thesis may be made electronically available to the public.

Statement of Contributions

Zi Jun Su was the sole author for Chapters 1, 2, and 6 which were written under the supervision of Dr. Slim Boumaiza and Dr. Patrick Mitran and were not written for publication.

This thesis includes four manuscripts that were submitted or published in Automatic RF Techniques Group (ARFTG) Microwave Measurement Conference or IEEE Transactions on Microwave Theory and Techniques.

Work presented in Chapter 3:

Publication I: This research was conducted at the University of Waterloo by Zi Jun Su under the supervision of Dr. Slim Boumaiza and Dr. Patrick Mitran. Zi Jun Su and Ahmed Ben Ayed implemented the digital signal processing of the frequency stitching methods in Matlab codes. Zi Jun Su and Ahmed Ben Ayed conducted the experiments, compiled the results and drafted the manuscript.

Citation:

Z. J. Su, A. Ben Ayed and S. Boumaiza, "Wideband Vector Signal Generation Using Multiple Narrowband Phase-Coherent Synchronous Signal Channels," 2024 103rd ARFTG Microwave Measurement Conference (ARFTG), Washington, DC, USA, 2024, pp. 1-4, doi: 10.1109/ARFTG61196.2024.10660844.

Publication II: This research was conducted at the University of Waterloo by Zi Jun Su under the supervision of Dr. Slim Boumaiza and Dr. Patrick Mitran. Zi Jun Su conducted the experiments and compiled the results. Zi Jun Su and Nizar Messaoudi drafted the manuscript. Ahmed Ben Ayed reviewed and edited the manuscript.

Citation:

Z. J. Su, N. Messaoudi, A. Ben Ayed, J. -P. Teyssier and S. Boumaiza, "Comparison of Signal Generation Approaches for Component Testing at D-Band," 2024 103rd ARFTG Microwave Measurement Conference (ARFTG), Washington, DC, USA, 2024, pp. 1-4, doi: 10.1109/ARFTG61196.2024.10660848.

Work presented in Chapter 4:

Publication III: This research was conducted at the University of Waterloo by Zi Jun Su under the supervision of Dr. Slim Boumaiza and Dr. Patrick Mitran. Ahmed Ben Ayed conceptualized the calibration technique. Zi Jun Su and Ahmed Ben Ayed implemented the calibration technique into Matlab codes. Zi Jun Su and Ahmed Ben Ayed conducted the

experiments, compiled the results and drafted the manuscript. Nizar Messaoudi reviewed and edited the manuscript.

Citation:

Z. J. Su, A. Ben Ayed, N. Messaoudi, P. Mitran and S. Boumaiza, "Frequency-Stitching-Based Ultrawideband Signal Generation for 6G Component/System Testing: Achieving 12-GHz Instantaneous Bandwidth and 96-Gbps Data Rate at D Band," in IEEE Transactions on Microwave Theory and Techniques, doi: 10.1109/TMTT.2024.3487823.

Work presented in Chapter 5:

Publication IV: This research was conducted at the University of Waterloo by Zi Jun Su under the supervision of Dr. Slim Boumaiza and Dr. Patrick Mitran. Zi Jun Su proposed the two architectures for the comparative study. Ahmed Ben Ayed performed the simulation of the architectures in Matlab. Zi Jun Su and Ahmed Ben Ayed conducted the experiments, compiled the results and drafted the manuscript.

Citation:

Z. J. Su, A. Ben Ayed, P. Mitran and S. Boumaiza, "Comparative Study of Two Architectures Suitable for the Generation of Wideband Signals at Sub-THz", 2025 104th ARFTG Microwave Measurement Conference (ARFTG). [Accepted]

As lead author of these chapters, I was responsible for contributing to implementing the theory, conducting the experiments, and drafting and submitting manuscripts. My coauthors provided guidance and feedback during each step of the research.

Abstract

The rise of sixth-generation (6G) wireless technology has created a need for wideband signal generation at high radio frequencies (RF). However, current digital-to-analog converters (DACs) face limitations, offering either wide bandwidth with low resolution or high resolution with limited bandwidth. This thesis proposes two methods that utilize multiple DACs to generate multiple narrowband sub-bands of a wideband signal, that are combined to produce the desired wideband signal. These methods employ distinct digital processing approaches tailored to specific applications, such as instrumentation or real-time Orthogonal Frequency Division Multiplexing (OFDM) signal generation.

To address non-idealities in frequency-stitching-based transmitters, a frequency-domain calibration technique using multi-tone signals is introduced. Experiments at X-band (9.6 GHz) and D-band (129.6 GHz) validate these methods, demonstrating up to 8 GHz bandwidth and achieving an error vector magnitude (EVM) as low as 0.3% for a 7.2 GHz 256-QAM OFDM signal. A comparative study of three signal generation approaches—direct Arbitrary Waveform Generator (AWG) generation, baseband in-phase and quadrature (IQ) generation with up-conversion, and frequency stitching—shows EVMs of 1.5%, 0.8%, and 1%, respectively, for an 8 GHz OFDM signal.

A novel architecture using phase-coherent IQ-DACs and mixers for each sub-band is also presented. Calibration using non-uniformly interleaved tones corrects IQ imbalances and distortions, enabling the generation of a 256-QAM OFDM signal with 12 GHz bandwidth at D-band (149 GHz) and achieving a peak data rate of 96 Gbps. Calibration improves EVM and normalized mean square error (NMSE) from 82.6% and 23.8% to below 2% and 1%, respectively. Additionally, D-band amplifier linearization with a 4 GHz modulation bandwidth improves adjacent channel power ratio (ACPR) from -27.8/-26 dBc to -42.8/-43.1 dBc and EVM from 8.5% to 1.2%.

Finally, two architectures for sub-band combination are compared. One generates a wideband signal at intermediate frequency (IF) and up-converts it, while the other up-converts narrowband IF signals and combines them. The second approach demonstrates superior ACPR at high IF power levels, enhancing ACPR by up to 8 dB when generating a 1.2 GHz modulated signal at 142.5 GHz.

These results highlight the efficacy of the proposed methods for generating and linearizing high-quality wideband signals, supporting advanced applications in millimeter wave and sub-THz frequency bands for 6G technologies.

Acknowledgements

I would like to thank my supervisors Professor Slim Boumaiza and Professor Patrick Mitran for their invaluable guidance, support, and encouragement throughout this journey. Their patience, insight, and constructive feedback have been instrumental in shaping this research and in my academic growth.

Special thanks go to my fellow EmRG members, who provided support, inspiration, and camaraderie during the more challenging moments of this process. The shared discussions and collaborative spirit made this experience all the more meaningful.

Lastly, I would like to thank my family for their unconditional love, patience, and unwavering belief in my abilities. Their encouragement has been a constant source of motivation.

Table of Contents

Author's Declaration ii

Statement of Contributions iii

Abstract v

Acknowledgements vi

List of Figures x

1 Introduction 1

2 Background 4

2.1 Signal Quality Metrics 4

2.1.1 Error Vector Magnitude 5

2.1.2 Normalized Mean Square Error 6

2.1.3 Adjacent Channel Power Ratio 6

2.2 Signal Generation Architecture 8

2.2.1 IF Signal Generation Stage 8

2.2.2 Upconversion Stage 10

2.3 Literature Review on Wideband Signal Generation 12

2.3.1 Stitching Based Signal Generation 12

2.3.2 High-Speed DAC Signal Generation . . . 15
2.4 Literature Review on Calibration for Transmitter Architectures . . . 16
2.4.1 Components Frequency Response Calibration . . . 16
2.4.2 IQ Imbalance Calibration . . . 16
2.4.3 Calibration for Time Interleaving Signal Generation Method . . . 17
2.4.4 Calibration for Frequency Stitching Signal Generation Method . . . 18

3 Signal Generation Using Frequency Stitching Methods 21
3.1 Transmitter Stitching Formulation . . . 22
3.1.1 Proposed wideband signal generation utilizing Frequency-Stitching and periodic signals . . . 22
3.1.2 Proposed real-time wideband signal generation tailored for OFDM signals and utilizing frequency-stitching . . . 22
3.1.3 Wideband Frequency Domain Calibration . . . 24
3.2 Experimental Validation . . . 25
3.2.1 Measurement Setup . . . 25
3.2.2 Measurement Results . . . 25
3.3 Comparison with Other Wideband Signal Generation Methods . . . 29
3.3.1 Measurement Setup . . . 29
3.3.2 Measurement Results . . . 29
3.4 Conclusion . . . 32

4 Frequency Stitching Applied to IQ DAC and IQ Mixer Signal Generation Architecture 33
4.1 Calibration Formulation . . . 34
4.2 Experimental Validation . . . 39
4.2.1 Measurement Setup . . . 39
4.2.2 Measurement Results . . . 41
4.3 Conclusion . . . 43

5 Comparison Study of IF Combining and RF Combining Architecture for Using Frequency Stitching in Signal Generation **48**

5.1 Comparative Analysis of the IF and RF Combining Architectures 49

5.1.1 Noise Limited Analysis 50

5.1.2 Non-linearity Distortion Limited Analysis 51

5.2 Simulation for the IF and RF Combining Architecture 53

5.3 Experimental Validation 53

5.3.1 Measurement Setup 53

5.3.2 Measurement Results 54

5.4 Conclusion 56

6 Conclusion **58**

6.1 Future Work 59

6.1.1 DPD for Nonlinearity in Upconverter 59

6.1.2 DPD for Nonlinearity from Different Sub-Bands 60

References **61**

List of Figures

1.1 Usage scenarios for 6G by the International Telecommunications Union for 2030 and beyond [27]. 2

2.1 EVM vs operating power. 5
2.2 IM distortion components of a nonlinear system. 7
2.3 Diagram of a generic transmitter architecture. 9
2.4 Diagram of homodyne architecture, and the distortions in the signal generated. 10
2.5 Diagram of heterodyne architecture, and the limitation of signal bandwidth in the signal generated. 11
2.6 Spectrum at the output of the mixer that uses frequency multiplier for LO: (top) the undesired image signals in red are under the desire signal in blue; (bottom) the undesired signals does not overlap with the desire signal, and were filtered out using BPF. 13
2.7 Diagram of time interleaved DACs [10]. 14
2.8 Diagram of frequency stitching operation [3]. 15
2.9 Simulation results of generating a sinusoid wave using time interleaving DACs, with calibration applied (left) and without calibration applied (right) 17
2.10 Phase detector circuit for clock alignment of time interleaving DACs [12]. . 18
2.11 Compensation method for LO leakage in frequency stitching signal generation architecture [3]. 19
2.12 Calibration signal for two DAC paths for the phase offset calibration [18]. . 19

3.1 System diagram of the proposed frequency-stitching methods, (Top) for periodic signal measurements and (Bottom) for real-time application. 23

3.2 Measurement setup. 26

3.3 Measured PSD (Left) and constellation (Right) of a 256-QAM 8 GHz bandwidth OFDM signal centered at 9.6 GHz, generated using the proposed Method-1 with four RF-AWG channels: a) before transmitter calibration, and b) with the proposed calibration technique applied. 26

3.4 Measured PSD (Left) and constellation (Right) at an X-band amplified output driven with a 256-QAM 2.6 GHz bandwidth OFDM signal centered at 9.6 GHz, generated using the proposed Method-1 with four RF-AWG channels: a) before linearization applied; b) with linearization applied. . . . 27

3.5 Measured PSD (Left) and constellation (Right) of a 256-QAM 4 GHz bandwidth OFDM signal centered at 129.6 GHz, generated using the proposed Method-1 with two RF-AWG channels: a) before transmitter calibration; b) with transmitter calibration applied. 28

3.6 Measured PSD (Left) and constellation (Right) of a 256-QAM 7.6 GHz bandwidth OFDM signal centered at 9.6 GHz, generated using the proposed Method-2 with four RF-AWG channels: a) before transmitter calibration; b) with transmitter calibration applied. 28

3.7 Block diagram of the measurement setup. 30

3.8 Measured PSD (Left) and constellation (Right) of a 256-QAM 8 GHz bandwidth OFDM signal centered at 158.4 GHz, through test, generating using equipment and method: a) M8199A; b) M8190A with IQ mixer; c) M5300A using channel bonding. 31

3.9 Measured PSD (Left) and constellation (Right) at a D-Band amplifier of a 256-QAM 2.6 GHz bandwidth OFDM signal centered at 158.4 GHz, linearizing with ILC: a) before linearization; and after linearization for the three signal generation approaches: b) M8199A; c) M8190A with IQ mixer; d) M5300A using channel bonding. 31

4.1 Equivalent complex baseband representation of the proposed frequency-stitching ultra-wideband signal generator, illustrating non-idealities and calibration filters. 34

4.2 Conceptual diagram of the effects of IQ imbalance on the generated signal in a two-channel frequency-stitching signal generator (i.e., $P = 2$). The figure also showcases the proposed non-uniformly interleaved calibration signal. . 38

4.3 Block diagram of the D-band measurement setup used to validate the proposed frequency-stitching based signal generation method. 39

4.4 Measured PSD at D-band of a 256-QAM 12 GHz bandwidth OFDM signal generated using the proposed method: a) before calibration, and b) with the proposed calibration applied. 42

4.5 Measurend constellation at D-band of a 256-QAM 12 GHz bandwidth OFDM signal generated using the proposed method: a) before calibration, and b) with the proposed calibration applied. 43

4.6 Measured PSD of the error signal at D-band of a 256-QAM 12 GHz bandwidth OFDM signal generated using the proposed method: a) before calibration, and b) with the proposed calibration applied. 44

4.7 Measured PSD at D-band of a 256-QAM 4 GHz bandwidth OFDM signal generated using the proposed method with the PA bypassed: a) before calibration, and b) with the proposed calibration applied. 45

4.8 Measured PSD at the D-band PA output when driven with a 256-QAM 4 GHz bandwidth OFDM signal: a) before linearization with calibration applied, and b) after linearization with calibration applied. 45

4.9 Measured constellation at the D-band PA output when driven a 256-QAM 4 GHz bandwidth OFDM signal: a) before linearization with calibration applied, and b) after linearization with calibration applied. 46

4.10 Measured gain distortion at the D-band PA output when driven with a 256-QAM 4 GHz bandwidth OFDM signal: a) before linearization with calibration applied, and b) after linearization with calibration applied. . . . 46

4.11 Measured phase distortion at the D-band PA output when driven with a 256-QAM 4 GHz bandwidth OFDM signal: a) before linearization with calibration applied, and b) after linearization with calibration applied. . . . 47

5.1 Functional block diagram of wideband signal generation at Sub-THz frequencies using frequency bonding, (top) at IF, (bottom) at sub-THz. . . . 49

5.2 Simulated ACPR as a function of power sweep for: (a) IF combining architecture before linearization, (b) after linearization, (c) RF combining architecture before linearization, and (d) after linearization. 53

5.3 Measurement setup. 55

5.4 Measured ACPR as a function of power sweep for: (a) the IF combining architecture before linearization, (b) after linearization, (c) the RF combining architecture before linearization, and (d) after linearization. 55

5.5 Measured EVM as a function of power sweep for: (a) the IF combining architecture before linearization, (b) after linearization, (c) the RF combining architecture before linearization, and (d) after linearization. 56

5.6 Power spectral density of the signal at an RF power of -10 dBm, generated using: (a) the IF combining architecture before linearization, (b) after linearization, (c) the RF combining architecture before linearization, and (d) after linearization. 57

Chapter 1

Introduction

The rapid evolution of wireless communication has led to an escalating demand for higher data rates and more robust connectivity. Fourth-generation (4G) networks deployed in the 2010s, supports peak data rates of around 1 gigabit per second (Gbps). In contrast, fifth-generation (5G) networks, deployed in 2020s, have increased the peak data rates to 20 Gbps. Currently, sixth-generation (6G) networks are under development, with targeted peak data rates between 100 and 200 Gbps [28, 27]. This progression toward higher data rates and more extensive connectivity across network generations has enabled numerous new applications, as each generation brings improved capacity, reliability, and user experience.

However, while 5G has made significant strides in enhancing data rates and supporting applications such as high-definition video, self-driving cars, and smart cities, it faces limitations in terms of capacity, energy efficiency, and latency. As shown in Fig. 1.1, to address these limitations, 6G is being developed to push the boundaries even further, with extreme requirements for data rates, ultra-low latency, energy efficiency, and reliability. 6G seeks to enhance existing 5G usage scenarios, including Enhanced Mobile Broadband, ultra-reliable low-latency communication, and massive machine-type communication. Beyond these, 6G networks are designed to support transformative use cases in artificial intelligence (AI)-driven applications, integrated sensing and communication, and ubiquitous connectivity [27]. For instance, AI-driven applications in 6G could support real-time digital twins, enabling the simulation, management, and predictive control of complex systems across various industries [16]. Integrated sensing and communication can enhance autonomous systems for applications like automated driving and drone-based logistics, where seamless data exchange and environmental sensing are critical for safe and efficient operations. Lastly, ubiquitous connectivity in 6G is expected to power massive-scale Internet of Things (IoT) deployments, such as smart cities and environmental monitoring

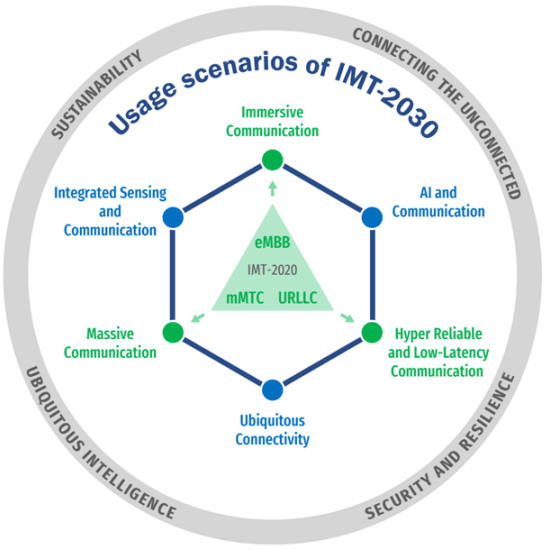


Figure 1.1: Usage scenarios for 6G by the International Telecommunications Union for 2030 and beyond [27].

systems, where billions of connected devices communicate and share data continuously.

To achieve these ambitious performance targets, 6G networks will, compared to 5G networks, rely on enhanced capabilities, such as achieving a latency in the range of 0.1 to 1 ms, supporting up to 10^6 to 10^8 devices per square kilometer, and enhancing spectral efficiency by leveraging higher frequency bands. Furthermore, there is a critical need for increased energy efficiency to handle the rising power demands of massive data transmission. Meeting these stringent capabilities is essential to enable applications such as real-time digital twins, autonomous driving, and smart cities [27].

One of the fundamental challenges in achieving 6G's high data rates is the need for significantly wider bandwidths. According to the Shannon-Hartley theorem,

$$C = B \log_2(1 + SNR). \tag{1.1}$$

Where C is the channel capacity, and B is the bandwidth. Higher order modulation schemes require higher SNR to maintain a acceptable bit error rate (BER). For instance, a 256 quadrature amplitude modulation (QAM) modulation scheme would require an SNR of more than 35 dB without any error correction [19]. To support a 256 QAM signal with a peak data rate of 100 Gbps, a bandwidth of approximately 8 GHz is needed. Due to the crowded sub-6 GHz spectrum, higher frequencies, specifically in the millimeter wave

(mmWave) and sub-terahertz (sub-THz) bands (30 to 300 GHz), are now prime candidates for generating these wideband signals.

Generating wideband signals presents several technical challenges, particularly in the design of digital-to-analog converters (DACs). For example to achieve 8 GHz modulation bandwidth, the DACs must have sampling rates of at least 16 Gsps per the Nyquist theorem. Additionally, the DACs must ensure sufficient SNR to meet emission mask requirements, which often necessitates high resolution and additional SNR margins to compensate for noise introduced by other components, such as power amplifiers (PAs) and antennas.

To address these challenges, this thesis proposes two frequency stitching methods for use in laboratory testing or real-time environments. In both methods, the signal is digitally partitioned into sub-bands, with each sub-band generated by a separate DAC. These sub-band signals are then combined using a Wilkinson power combiner. The frequency stitching methods are applied to different signal generation architectures, and calibration methods are introduced to mitigate distortion introduced during the stitching process.

This thesis is organized as follows: Chapter 2 discusses signal quality evaluation metrics, transmitter architectures, and a review of prior work on wideband signal generation. Chapter 3 presents two proposed frequency stitching methods and experimental results using RF-DACs. Chapter 4 explores frequency stitching with IQ-DACs for achieving even wider bandwidth and introduces a calibration method for multiple IQ-DACs. Chapter 5 presents a comparative study on the performance of combining sub-band signals at intermediate frequency (IF) or after upconversion to radio frequency (RF). Finally, Chapter 6 provides a summary and potential directions for future research.

Chapter 2

Background

This chapter addressed key considerations for wideband signal generation in 6G networks. It begins with a discussion of essential signal quality evaluation metric that play a vital role in identifying potential sources of distortion within the signal. Next, signal generation architectures are presented, highlighting the advantages and limitations of each. A literature review of existing methods for extending the signal bandwidth is provided. However, many of these methods are either unsuitable or have not been validated for application to 6G signal generation. To address this gap, two frequency-stitching-based signal generation methods are proposed to meet the stringent requirements of 6G networks, and measurements are conducted to validate these methods. Additionally, a literature review of calibration techniques for mitigating distortions is presented. Proper calibration routines are critical to ensure accurate measurements with minimal distortion.

2.1 Signal Quality Metrics

For a receiver to receive a signal and extract the information contained in the signal, the transmitter must ensure that the generated signal is of sufficient quality. There are various metrics that characterize the signal in an RF communication system. These metrics can measure, at different stages of the system, how much distortion is added by each stage, and help develop methods to mitigate the distortion.

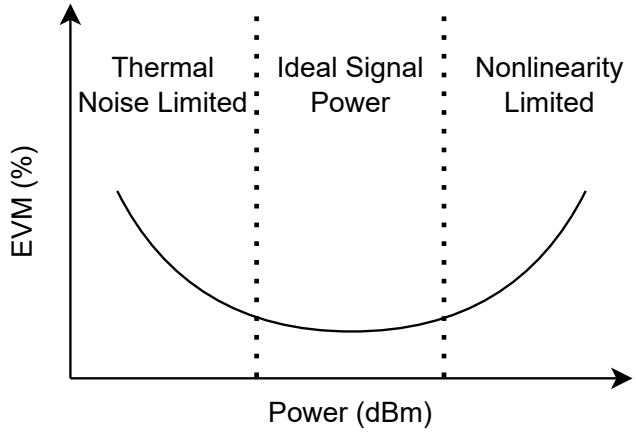


Figure 2.1: EVM vs operating power.

2.1.1 Error Vector Magnitude

Error Vector Magnitude (EVM) is a widely used metric for assessing signal quality in systems employing digital modulation. A modulated signal can be represented on a constellation diagram, where EVM quantifies the deviation of the received symbol from its ideal position in the diagram. This deviation serves as a measure of the fidelity of the signal. Each modulation scheme has specific EVM requirements. For instance, in 3GPP, 256-QAM requires an EVM below 3.5%. High EVM values often indicate issues such as in-phase (I) and quadrature (Q) imbalance, low signal-to-noise ratio (SNR), or nonlinearities caused by components such as amplifiers.

At low power levels, EVM is predominantly limited by thermal noise. Thermal noise combined with low signal power results in reduced SNR, with the relationship between SNR and EVM expressed as:

$$SNR = -[PAPR + 20 \times \log_{10}^{EVM_{\%}/100}]. \tag{2.1}$$

At high power levels, system components can exhibit nonlinear behavior, introducing nonlinear distortion that degrades EVM. When EVM is plotted against operating power, the result is typically a "bathtub curve," as illustrated in Fig. 2.1.

In systems employing Orthogonal Frequency Division Multiplexing (OFDM), EVM is

calculated using the following equation:

$$\mathrm{EVM} = \frac{\sum_{k=0}^{K_\mathrm{D}} \left|\tilde{y}_\mathrm{FFT}(v_k) - \tilde{d}_\mathrm{FFT}(v_k)\right|^2}{\sum_{k=0}^{K_\mathrm{D}} \left|\tilde{d}_\mathrm{FFT}(v_k)\right|^2}, \tag{2.2}$$

where, $\tilde{y}_\mathrm{FFT}$ and $\tilde{d}_\mathrm{FFT}$ are the discrete-time Fourier transform of the received and ideal signals, respectively. Furthermore, K_D is the total number of sub-carriers, v_k is the k^{th} sub-carrier discrete-time Fourier transform index.

In most cases, the reported EVM value is measured after equalization. During this process, pilot symbols are aligned with their ideal positions on the constellation diagram, and the remaining points are shifted accordingly. Equalization effectively mitigates most linear distortions, ensuring that the EVM reflects only nonlinear effects and residual noise.

2.1.2 Normalized Mean Square Error

Normalized Mean Square Error (NMSE) is a metric used to evaluate how closely the received signal matches the ideal signal. While NMSE and Error Vector Magnitude (EVM) often yield similar values, they differ in scope: EVM quantifies the error after signal demodulation, whereas NMSE assesses the error in the time or frequency domain.

In most scenarios, NMSE and EVM values are comparable. However, when linear distortion is present in the system, NMSE tends to be more adversely affected, resulting in a worse value than EVM. For this reason, both NMSE and EVM are measured in experiments to help identify and distinguish the types of distortion affecting the system. Beyond linear distortion, high-power spurious emissions can also degrade the measured NMSE, further emphasizing its importance as a diagnostic tool.

2.1.3 Adjacent Channel Power Ratio

Adjacent Channel Power Ratio (ACPR) is a metric that compares the in-band signal power to the power of the out-of-band emissions. The out-of-band power must be measured using the same bandwidth as the in-band power. Therefore, the receiver needs to capture a bandwidth at least three times the signal bandwidth to perform this measurement accurately. ACPR is commonly used to evaluate nonlinearity in a system, as nonlinearity causes spectral regrowth, which manifests as distortion in the out-of-band spectrum.

Nonlinearity is often characterized using the two-tone test. When a two-tone signal is input to a nonlinear device, the output generates intermodulation (IM) components. In

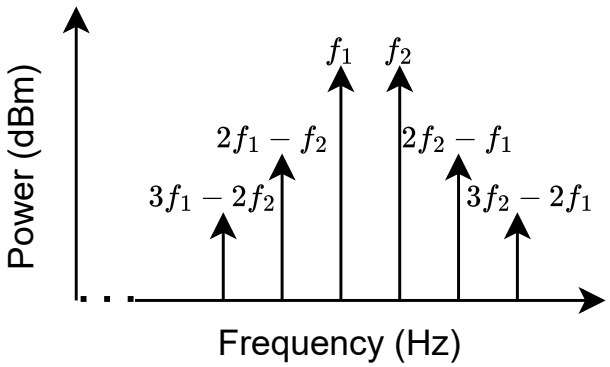


Figure 2.2: IM distortion components of a nonlinear system.

the frequency spectrum, let the two tones have frequencies f_1 and f_2 . The IM components are sum and difference products of these fundamental tones. For instance, second-order IM components include $f_1 + f_2$ and $f_1 - f_2$. Among these, some odd-order IM products appear very close to the fundamental tones, as shown in Fig. 2.2. When transmitting discrete multi-tone signals, these odd-order IM products collectively form spectral regrowth, causing distortion in adjacent frequency bands.

A common technique to mitigate nonlinear distortion is digital predistortion (DPD). DPD uses a feedback loop, often referred to as the transmitter observation receiver (TOR), to measure the nonlinearly distorted signal. The TOR output is then used to estimate coefficients for creating a predistorted signal, which is applied to the transmitter's input to compensate the distortion. Various models have been developed to estimate these DPD coefficients, including the General Memory Polynomial (GMP) model, the Dynamic Deviation Reduction (DDR) model [9], and the Complexity-Reduced Volterra (CRV) model [17]. Different nonlinear devices introduce varying forms of distortion, and specific DPD models are better suited to certain types of nonlinearity.

While DPD models are designed for real-time deployment, an alternative approach for laboratory testing is Iterative Learning Control (ILC). ILC is a straightforward and efficient method for reducing nonlinear distortion. It iteratively calculates the error between the received and ideal signals, then adjusts the signal to be generated accordingly. The ILC

process is described by the following equation:

$$\tilde{x}_{i+1}[n] = \tilde{x}_i[n] + \mu(\bar{x}_i[n] - \tilde{y}_i[n]), \tag{2.3}$$

Where i denotes the iterations, $\tilde{x}$ is the signal generated, $\bar{x}$ is the ideal signal, $\tilde{y}$ is the received signal, and μ is the error step size.

ILC is sometimes used as a benchmark for testing DPD models because it can produce nearly ideal results in reducing nonlinear distortion. While not practical for real-time deployment, ILC provides valuable insights for evaluating and refining DPD performance.

2.2 Signal Generation Architecture

To meet the latest communication standards, RF systems must operate at frequencies ranging from 30 GHz to 300 GHz, encompassing the mmWave and sub-THz bands. Achieving such high frequencies is challenging for conventional heterodyne or homodyne transmitters, necessitating an additional upconversion stage in the signal generation architecture.

Figure 2.3 illustrates a generic architecture for signal generation at mmWave and sub-THz frequencies. The architecture begins with signal generation at an intermediate frequency (IF) using either a heterodyne or homodyne architecture. The IF signal is then upconverted to RF within the mmWave or sub-THz range. During the upconversion process, the mixer generates an unwanted image signal alongside the desired signal. To suppress this image signal, a bandpass filter (BPF) is employed after the upconverter.

Following the BPF, the signal is amplified using a power amplifier (PA). The PA ensures that the transmitted signal has sufficient power to overcome the significant path loss encountered in high-frequency bands, enabling reliable reception at the receiver side.

2.2.1 IF Signal Generation Stage

There are two different architectures can be used for generating the IF signal: homodyne architecture and heterodyne architecture, each with their advantages and limitations.

Homodyne Architecture

The homodyne architecture employs two IQ-DACs to generate the I and Q baseband signals. Each DAC output is filtered using a low-pass filter (LPF) to suppress Nyquist

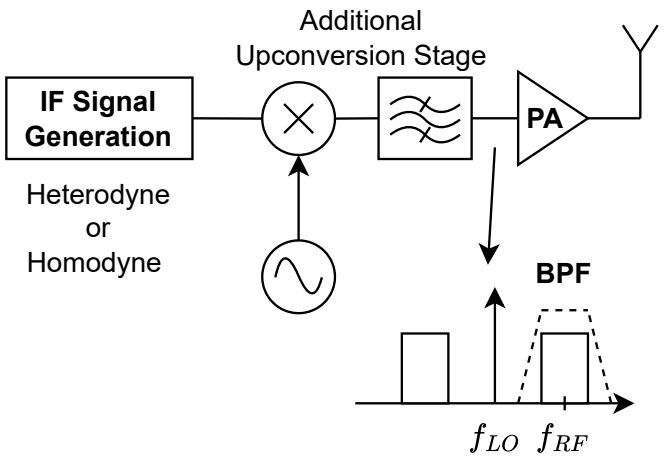


Figure 2.3: Diagram of a generic transmitter architecture.

images, and the I and Q signals are subsequently modulated to an IF signal using an IQ mixer. A block diagram of the homodyne architecture is shown in Fig. 2.4.

This architecture introduces distortions, primarily IQ imbalance and local oscillator (LO) feedthrough. IQ imbalance results in an image signal appearing at the same frequency as the desired signal, while LO feedthrough manifests as a tone at the center of the signal band, as illustrated in Fig. 2.4. These distortions can be mitigated through IQ imbalance calibration and incorporating a bias-tee to lower the power of the tone created by LO feedthrough. However, such corrective measures increase both computational complexity and the form factor of the system.

Heterodyne Architecture

The heterodyne architecture performs the IQ modulation digitally. Following the IQ modulation, one RF-DAC is used to generate the signal at a lower frequency. An LPF is applied to suppress Nyquist images from the RF-DAC output. The resulting signal is then upconverted to IF. After upconversion, a BPF is used to filter the image signal due to the mixer. Figure 2.5 provides a block diagram of this architecture.

Compared to the homodyne architecture, the heterodyne approach avoids IQ imbalance

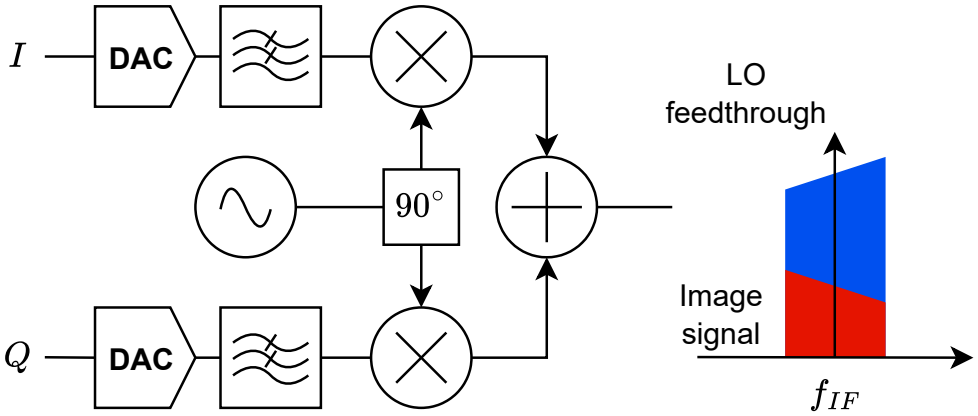


Figure 2.4: Diagram of homodyne architecture, and the distortions in the signal generated.

and LO feedthrough distortions. However, it has notable trade-offs, including half the achievable signal bandwidth and a larger overall form factor.

In some setups, a high-speed RF-DAC is used. This allows the RF-DAC to generate the signal at IF directly, such that the upconversion in the heterodyne architecture can be removed. If the desired RF is on the lower end of the mmWave and sub-THz frequencies, some RF-DACs [26] are capable of generating the signal at RF directly, removing the need for any upconversion in the entire signal generation architecture. This setup offers advantages such as a reduced form factor and fewer components, which in turn minimizes potential distortion sources. However, high-speed RF-DACs typically have lower resolution, resulting in degraded signal-to-noise ratio (SNR) for the generated signal.

2.2.2 Upconversion Stage

Most DACs in the typical heterodyne or homodyne transmitter architectures are designed to generate signals up to 10 GHz [33, 14, 8, 6]. To achieve the RF at mmWave and sub-THz frequencies, the mixer for the additional upconversion stage in the signal generation architecture needs to have an LO reaching a similar frequency. However, directly generating a clean continuous wave (CW) at frequencies approaching 300 GHz is highly challenging. As a result, frequency multipliers are often employed to generate the required LO for mixer-based architectures.

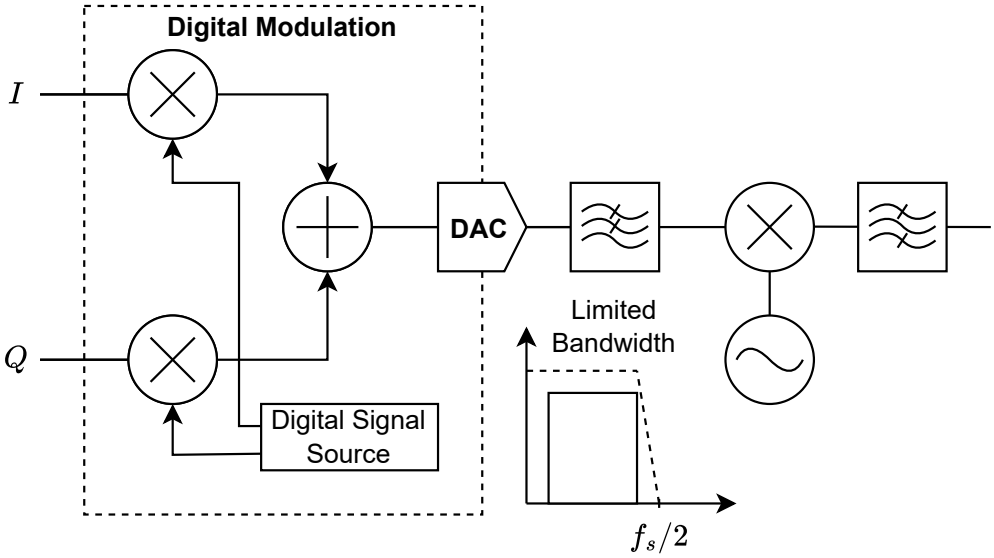


Figure 2.5: Diagram of heterodyne architecture, and the limitation of signal bandwidth in the signal generated.

Frequency multiplication involves introducing a nonlinearity to the CW signal, which generates harmonics at integer multiples of the CW frequency, $n \times f_{CW}$, where f_{CW} is the fundamental frequency. A bandpass filter (BPF) is then used to isolate the desired n^{th} order harmonic while attenuating unwanted harmonics and the fundamental tone. Different amount of nonlinear distortion will change the amplitude of the harmonic tones, therefore the amplitude of the desired harmonic can be optimize by varying the nonlinearity. Typically this distortion is achieve by passing the signal through components such as PAs operating in non-linear mode. A full wave rectifier circuit could also be used to achieve this distortion.

The mixer in the transmitter architecture upconverts the IF signal to RF by combining it with the LO signal, producing output frequencies at $f_{IF} + f_{LO}$ (desired signal) and $f_{IF} - f_{LO}$ (image signal). To suppress the image signal, a BPF is used after the mixer, as shown in Fig. 2.3. However, using a frequency multiplier for the LO introduces additional complications. Filtering the desired LO harmonic from the frequency multiplier output becomes increasingly difficult at high frequencies due to challenges in designing narrowband BPFs at such frequencies. Consequently, adjacent harmonics from the frequency multiplier may also mix with the IF signal, producing undesired image signals. As illustrated in Fig. 2.6 (top), improper selection of f_{IF} and f_{CW} can result in undesired image signals overlapping with the desired RF signal, causing distortion. To avoid this, the f_{CW} must be more than twice the signal bandwidth. This ensures sufficient spectral separation between the desired signal and image signals, achieving a cleaner RF spectrum as depicted in Fig. 2.6 (bottom).

2.3 Literature Review on Wideband Signal Generation

2.3.1 Stitching Based Signal Generation

In the literature, research has been conducted on using multiple DACs in parallel to generate wideband signals. By leveraging multiple DACs, the effective sampling rate is increased, allowing for an extension of the signal bandwidth. There are two primary approaches to achieve this: time interleaving and frequency stitching.

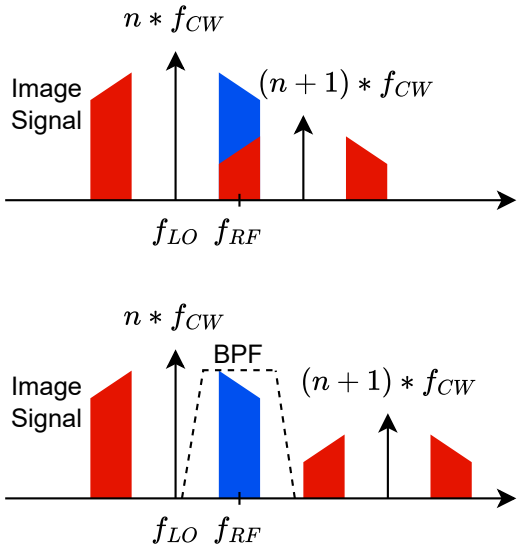


Figure 2.6: Spectrum at the output of the mixer that uses frequency multiplier for LO: (top) the undesired image signals in red are under the desire signal in blue; (bottom) the undesired signals does not overlap with the desire signal, and were filtered out using BPF.

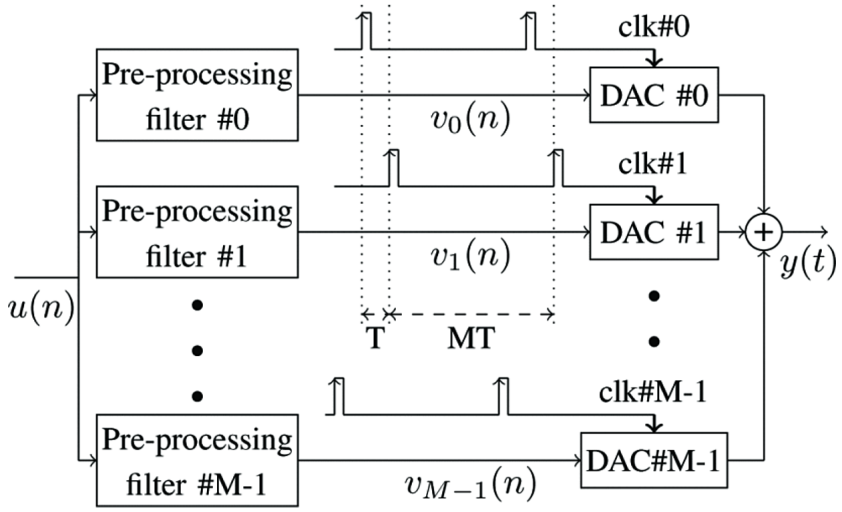


Figure 2.7: Diagram of time interleaved DACs [10].

Time Interleaving

The time interleaving method, introduced in [13, 11, 10, 12, 4, 31], employs multiple DACs operating in a staggered manner to increase the effective sampling rate. As illustrated in Fig. 2.7, with n DACs, each DAC generates signal samples at different time intervals, resulting in an overall sampling rate that is n times higher than a single DAC. This increased sampling rate enables the generation of signals with significantly wider bandwidths.

However, time interleaving suffers from sensitivity to timing mismatches. Any misalignment in the timing of the DACs introduces spurious tones in the spectrum, manifesting as unwanted frequency components. These distortions degrade the signal quality and require sophisticated calibration techniques to mitigate.

Frequency Sitiching

An alternative approach is frequency stitching, as discussed in [5, 21, 3, 18, 7]. The frequency stitching approach was illustrated in Fig. 2.8. In this method, the signal is first divided into multiple sub-bands in the frequency domain. Each sub-band is then generated separately using a dedicated DAC, allowing each DAC to handle a narrower bandwidth. These sub-band signals are upconverted to distinct frequency bands and then combined to form a single wideband signal.

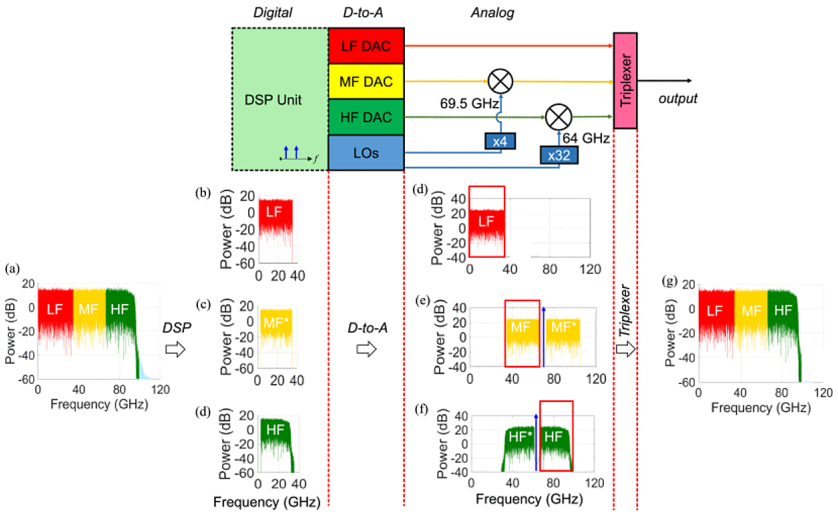


Figure 2.8: Diagram of frequency stitching operation [3].

While frequency stitching avoids the timing sensitivity issues of time interleaving, it introduces its own challenges. The upconversion process produces image signals due to the nature of the frequency mixing operation. Notably, the IQ signal generation architecture is a specific example of frequency stitching, where two DACs generate in-phase (I) and quadrature (Q) components of the signal, which are then combined to form the signal.

2.3.2 High-Speed DAC Signal Generation

Another approach for wideband signal generation is to use high-speed DACs. Advances in DAC technology have enabled the development of DACs with extremely high sampling rates, thereby increasing the achievable bandwidth for signal generation. As shown in Fig. 2.5, the signal bandwidth is limited by the Nyquist frequency, $f_s/2$. Therefore, increasing the sampling rate of a DAC allows for wider bandwidth signal generation. Several studies [20, 30, 32] have demonstrated the use of high-speed DACs for wideband signal measurements.

However, using high-speed DACs introduces a trade-off. Higher sampling rates often come at the cost of reduced resolution (fewer bits per sample), which degrades the signal-to-noise ratio (SNR) and increases quantization noise. This trade-off must be carefully considered when selecting a signal generation method, especially in systems that demand high signal fidelity.

2.4 Literature Review on Calibration for Transmitter Architectures

Transmitter architectures are subject to various forms of distortion that degrade signal quality. Key sources of linear distortion include the frequency response of components, IQ imbalance in IQ signal generation, and distortions introduced during the stitching process in frequency-stitching-based signal generation methods. To mitigate these distortions, various calibration routines have been developed, many of which employ a feedback structure similar to the TOR structure used in digital predistortion (DPD) systems.

2.4.1 Components Frequency Response Calibration

An ideal component would exhibit a consistent gain across its designed frequency range. However, in reality, manufacturing variations and inherent design limitations prevent this ideal behavior. The resulting frequency-dependent gain variation introduces signal distortion, necessitating calibration to achieve a near-ideal response. The most widely used approach for frequency response calibration is equalization. This technique involves approximating the inverse of the component's frequency response and applying it to the transmitted signal. By applying equalization, gain fluctuations are compensated, resulting in a more uniform output. This calibration is essential in wideband signal generation, where gain variations are more pronounced due to the broader frequency range.

2.4.2 IQ Imbalance Calibration

In IQ-based signal generation, IQ imbalance occurs due to mismatches in the amplitude and phase of the in-phase (I) and quadrature (Q) signals. These imbalances generate unwanted image signals that degrade the signal quality. A common solution for IQ imbalance distortion is adaptive interference cancellation using the Least Mean Square (LMS) algorithm. This method estimates the interference caused by the imbalance and subtracts it from the ideal signal. The LMS algorithm iteratively adjusts the filter coefficients to minimize the mean square error (MSE) between the ideal and received signals. Described in [29, 15], this approach allows the system to converge to an optimal filter that cancels the interference. Once the filter reaches a steady state, it effectively removes the IQ imbalance-induced distortion from the signal.

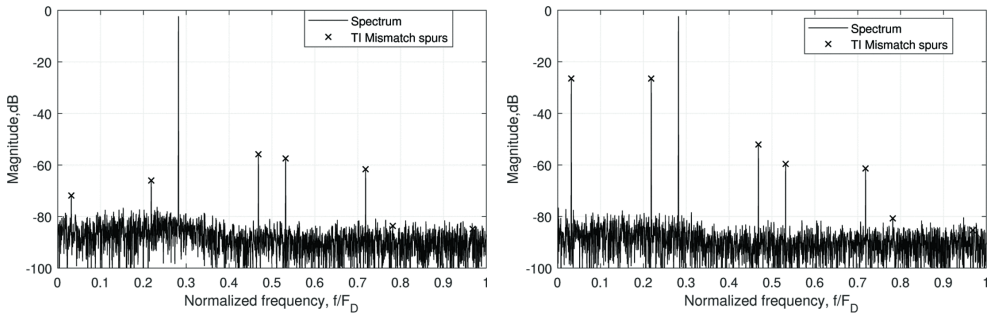


Figure 2.9: Simulation results of generating a sinusoid wave using time interleaving DACs, with calibration applied (left) and without calibration applied (right)

2.4.3 Calibration for Time Interleaving Signal Generation Method

In time-interleaved DACs, multiple DACs operate at staggered time intervals to achieve a higher effective sampling rate. However, clock mismatches between the DACs introduce timing errors that generate unwanted spurious tones in the signal spectrum. The following two approaches have been proposed to address this issue.

Pre-Processing Filter Calibration

A method for mitigating distortions from DAC mismatch is proposed in [10]. It involves the use of a pre-processing filter. This filter is computed by transmitting a known signal through the system, capturing the distorted output, and then calculating the inverse filter required to correct the signal. The process is similar to the adaptive interference cancellation used for IQ imbalance. Fig. 2.9 illustrates the impact of this calibration method. The simulation results show that, after applying the pre-processing filter, the spurious tones caused by clock mismatches are reduced by more than 30 dB, significantly improving signal quality.

Clock Alignment Using Phase Detector Circuit

Another approach to mitigate clock mismatch is to align the clocks of the DACs. As proposed in [12], this method uses a phase detector circuit to measure the overlap between two clocks and adjust the delay accordingly to achieve alignment. Fig. 2.10 shows the phase detector circuit. The circuit detects when the two clock signals have maximum

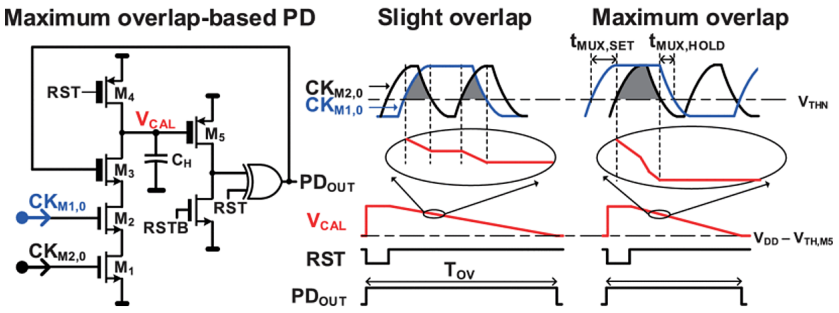


Figure 2.10: Phase detector circuit for clock alignment of time interleaving DACs [12].

overlap, which corresponds to a minimal high-state period at the circuit's output. A counter measures this high-state period, and the system uses the measurement to adjust the clock delay. While effective, this method faces scalability challenges, as aligning more clocks requires additional phase detectors and larger physical space for the circuitry.

2.4.4 Calibration for Frequency Stitching Signal Generation Method

Compensating for LO Leakage and Image Signal using Conjugate Tones

For the calibration of frequency stitching method, [3] proposed to generate tones with same amplitude and opposite phase of the distortion tones within the signal band, to compensate for the LO leakage tone that falls within the signal band. As Fig. 2.11 shown, the LO leakage from one of the sub-bands will show in the adjacent band. Creating a tone with same amplitude and opposite phase of the LO leakage in the adjacent band will remove the LO leakage. The extra tone created for the LO leakage compensation will have a image due to upconversion, but the image tone is placed outside of the band and will be filtered by the multiplexer. The same method of creating compensation tones is applied for image signals due to mixing that falls within the band. The limitation of this compensation method is that the amplitude and phase of the distortion tones need to be measured for different test signals. This method also has limited scalability. The distortion from different sub-bands and LOs need to be measured separately to calculate their amplitude and phase.

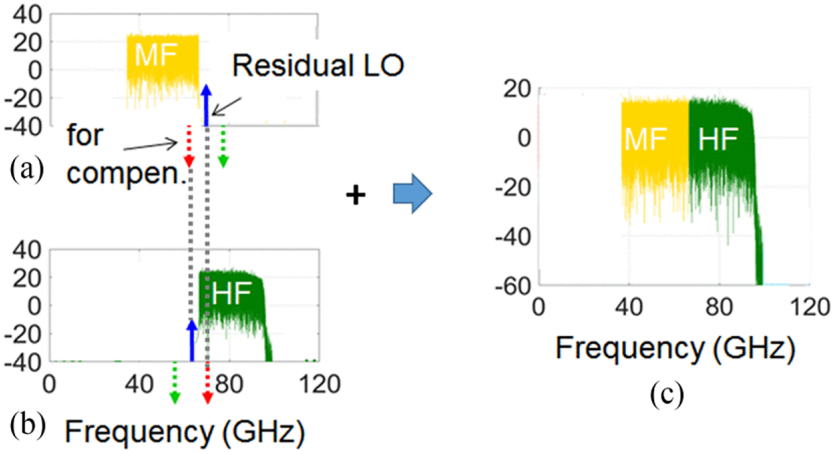


Figure 2.11: Compensation method for LO leakage in frequency stitching signal generation architecture [3].

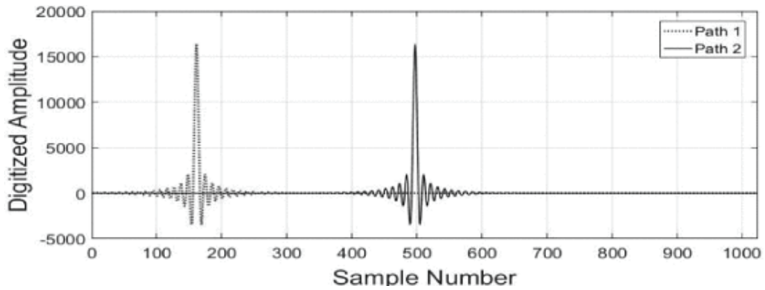


Figure 2.12: Calibration signal for two DAC paths for the phase offset calibration [18].

As a result, this method take a lot more time to calibrate when increasing the number of sub-bands.

Phase Offset Calibration

[18] proposed a calibration method for frequency stitching signal generation that includes mitigating phase offset between the different DAC path. The calibration signal for two DAC paths is illustrated in Fig. 2.12. This method generates the calibration signals with a delay between the two DAC paths, and receives the combined signal. The phase offset can be calculated using the delay in the received signal compared with the known delay applied to the DAC paths. The disadvantage of this method is that the calibration process is time consuming, as every DAC paths adds a delay to the combined receive signal.

Chapter 3

Signal Generation Using Frequency Stitching Methods

This chapter discusses the contribution from **Publication I** and **Publication II**. As discussed in the Chapter 2, generating wideband signals at mmWave and sub-THz frequencies presents significant challenges. While the existing literature explores methods such as channel bonding to generate wideband signals, these approaches have not yet been applied to meet the latest communication standards.

For this reason, this chapter introduces two frequency-stitching methods designed to address the challenges of wideband signal generation proposed in **Publication I**. The system diagram of the proposed signal generation methods is shown in Fig. 3.1. After a detailed formulation of these methods, their performance is validated through the generation of wideband signals, with signal quality assessed using the metrics discussed in the previous chapter.

Additionally, a comparative measurement is conducted to evaluate the performance of the proposed frequency-stitching methods against signal generation using an IQ DAC with an IQ mixer architecture, and signal generation using a single high-speed DAC, contribution form **Publication II**.

3.1 Transmitter Stitching Formulation

3.1.1 Proposed wideband signal generation utilizing Frequency-Stitching and periodic signals

In this sub-section, the theoretical formulation of the proposed frequency-stitching-based signal generation method for periodic signals, shown in Fig. 3.1 (Top), is presented. This method is referred to subsequently as Method-1. Let $\tilde{x}[n]$ be the wideband discrete-time complex baseband signal to be generated. In the following, the signal $\tilde{x}[n]$ is assumed to be periodic with period length N and sampling rate Fs. Accordingly, the signal $\tilde{x}[n]$ can be expressed as a function of its Fourier coefficients $\tilde{X}[k]$ as follows,

$$\tilde{x}[n] = \sum_{k=0}^{N-1} \tilde{X}[k] e^{j2\pi nk/N}. \tag{3.1}$$

To enable the generation of the wideband signal $\tilde{x}[n]$ using narrowband DACs, the signal $\tilde{x}[n]$ is partitioned into P sections, each section having a length of S. These partitions are then generated in parallel using narrowband DACs. Note, the periodicity of the signal prevents the occurrence of ISI that may arise from signal partitioning. The pth partition of $\tilde{x}[n]$, denoted as $\tilde{x}_p[n]$, can be expressed as,

$$\tilde{x}_p[n] = \sum_{k \in \mathcal{A}_p} \tilde{X}[k] e^{j2\pi nk/N}, \tag{3.2}$$

where the set $\mathcal{A}_p = \{p \times S, ..., (p+1) \times S - 1\}$. Note these partitions are non-overlapping such that,

$$\tilde{x}[n] = \sum_{p=0}^{P-1} \tilde{x}_p[n]. \tag{3.3}$$

3.1.2 Proposed real-time wideband signal generation tailored for OFDM signals and utilizing frequency-stitching

In this sub-section, the theoretical formulation of the proposed real-time wideband signal generation method tailored for OFDM signals and utilizing frequency-stitching, shown in Fig. 3.1 (Bottom), is presented. This method is referred to subsequently as Method-2. Let

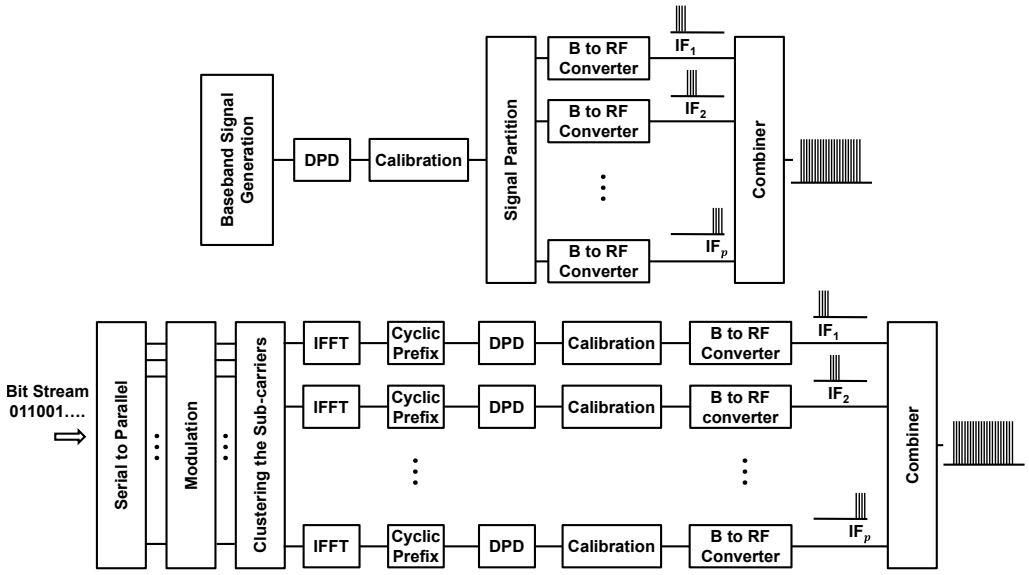


Figure 3.1: System diagram of the proposed frequency-stitching methods, (Top) for periodic signal measurements and (Bottom) for real-time application.

$(d_0, ..., d_{K_d})$ be a sequence of data symbols, where K_d is the number of symbols points. The OFDM symbol can be expressed as follows,

$$\tilde{s}[n] = \sum_{k=0}^{N_s-1} S[k] e^{j2\pi nk/N_s}, \tag{3.4}$$

Here, $S[k] = d_{k-\Omega_{K_d}(0)}$ for $k \in \Omega_{K_d}$ and zero otherwise. Ω_{K_d} represents the set of frequency indexes of the data symbols and a length equal to K_d, and $\Omega_{K_d}(0)$ denotes the first entry of the set Ω_{K_d}. Using the proposed scheme the set Ω_{K_d} is partitioned into P sets of equal length, $\Omega^p_{K_d}$, such that $\Omega_{K_d} = \cup_{p=0}^{P-0} \Omega^p_{K_d}$. Accordingly, the p'th partition of the OFDM symbol, $\tilde{s}_p[n]$, can be expressed as follows,

$$\tilde{s}_p[n] = \sum_{k \in \Omega^p_{K_d}} S[k] e^{j2\pi nk/N_s}. \tag{3.5}$$

Assuming a CP-OFDM type of modulation, the p'th generated signal $\tilde{x}_p[n]$ can be expressed as follows,

$$\tilde{x}_p[n] = \tilde{z}_p[n] * \tilde{T}[n], \tag{3.6}$$

where,

$$\tilde{z}_p[n] = \begin{cases} \tilde{s}_p[n - N + N_s] & n = N - N_s, ..., N - 1 \\ \tilde{s}_p[n - N + 2N_s - 1] & n = 0, ..., N - N_s - 1 \end{cases} \tag{3.7}$$

and $\tilde{T}[n]$ is the pulse shaping filter.

3.1.3 Wideband Frequency Domain Calibration

Due to nonidealities in the transmitter's RF front-ends, each partition of the wideband signal to be generated may undergo distinct non-ideal transfer functions, $\tilde{h}_p[n]$, varying time delay, m_p, and distinct phase offsets, ϕ_p, before their combination. Consequently, the non-ideal combined signal, $\bar{x}[n]$, can be expressed in discrete time complex baseband as follows,

$$\bar{x}[n] = \sum_{p=0}^{P-1} \tilde{h}_p[n] * \tilde{x}_p[n - m_p] e^{j\phi_p}. \tag{3.8}$$

Note, using phase-coherent synchronous sources guarantees that the phase offsets and delays are not time-varying. Alternatively, (3.8) can be expressed as a function of the ideal signal $\tilde{x}[n]$ as follows,

$$\bar{x}[n] = \tilde{h}[n] * \tilde{x}[n], \tag{3.9}$$

where,

$$\tilde{h}[n] = \sum_{p=0}^{P-1} \tilde{h}_p[n] * \delta[n - m_p] e^{j\phi_p}. \tag{3.10}$$

The objective of the calibration routine is to compensate for the linear nonidealities exhibited by the different RF chains in the transmitter and ensure proper reconstruction of the signal $\tilde{x}[n]$ at the combiner output. To that end, we assume that the signal $\tilde{x}[n]$ is a periodic calibration multi-tone signal, consequently (3.9) can be expressed in the frequency domain as,

$$\bar{X}[k] = \tilde{H}[k] \times \tilde{X}[k], \tag{3.11}$$

where $\bar{X}[k]$, $\tilde{H}[k]$, and $\tilde{X}[k]$ are the discrete Fourier coefficients of $\bar{x}[n]$, $\tilde{h}[n]$, and $\tilde{x}[n]$. Let Ω denote the frequency grid of the signal $\tilde{x}[n]$, such that $\tilde{X}[k] = 0$ for $k \notin \Omega$. The inverse frequency response $\tilde{G}[k]$ of $\tilde{H}[k]$ is then estimated by taking the ratio of $\tilde{X}[k]$ and $\bar{X}[k]$ for $k \in \Omega$ or setting $\tilde{G}[k]$ to one for $k \notin \Omega$. Finally, the inverse impulse response needed to calibrate the different chains, $\tilde{g}_p[n]$, can be obtained as follows,

$$\tilde{g}_p[n] = \sum_{k \in \mathcal{A}_p} \tilde{G}[k] e^{j2\pi nk/N}. \tag{3.12}$$

3.2 Experimental Validation

3.2.1 Measurement Setup

To validate the proposed wideband signal generation methods, the measurement setup shown in Fig. 3.2 was developed. The reported measurements were conducted at X-band and D-band frequencies. The signal source used for the experiments was a 14-bit, 2 GHz bandwidth, and 2.4 Gsps direct digital synthesis-based RF Arbitrary Waveform Generator (AWG) (M5300A from Keysight) with four synchronous phase-coherent channels. The outputs of the RF-AWG channels were connected to a power combiner and then routed to a VNA (N5242B from Keysight) and an X-band receiver for signal analysis. The X-band receiver consists of a downconverter (M5201A from Keysight) and a digitizer (M5200A from Keysight) and uses frequency-stitching technique to enable wideband signal analysis up 12 GHz. In the case of the D-band measurements, an upconverter was added to generate an RF signal at 129.6 GHz. The output of this upconverter was captured using a frequency-stitching-based receiver, comprising an VNA frequency extender (V06VNA1 from OML) and a digitizer (M5200A). The calibration routine was ran for 5 iterations for each measurement.

3.2.2 Measurement Results

Fig. 3.3 shows the power spectral density (PSD) (Left) and constellation (Right) of a 256-QAM 8 GHz bandwidth OFDM signal centered at 9.6 GHz, generated using the proposed Method-1 with four RF-AWG channels: a) before transmitter calibration, and b) with the proposed calibration technique applied. The root normalized mean squared error (RNMSE) and error vector magnitude (EVM) improved from 76.9% and 1.4% before calibration in (a) to 1% and 1% with calibration applied in (b), highlighting the effectiveness of the proposed signal generation scheme and calibration technique in achieving excellent signal quality with narrowband, high-bit resolution sources.

Building on these results, Method-1 was applied to linearize an X-band amplifier, enabling an 8 Hz linearization bandwidth. Fig. 3.4 presents the measured PSD (Left) and constellation (Right) at the amplifier output when driven with a 256-QAM 2.6 GHz bandwidth OFDM signal: a) before linearization with proposed calibration applied, and b) after linearization with proposed calibration applied. The EVM and adjacent channel power ratio (ACPR) improved from -33.5/-32.9 dBc and 6.4% before linearization in (a), to -51.3/-50.5 dBc and 1.2% after linearization in (b), confirming the excellent SNR performance of the proposed signal generation method.

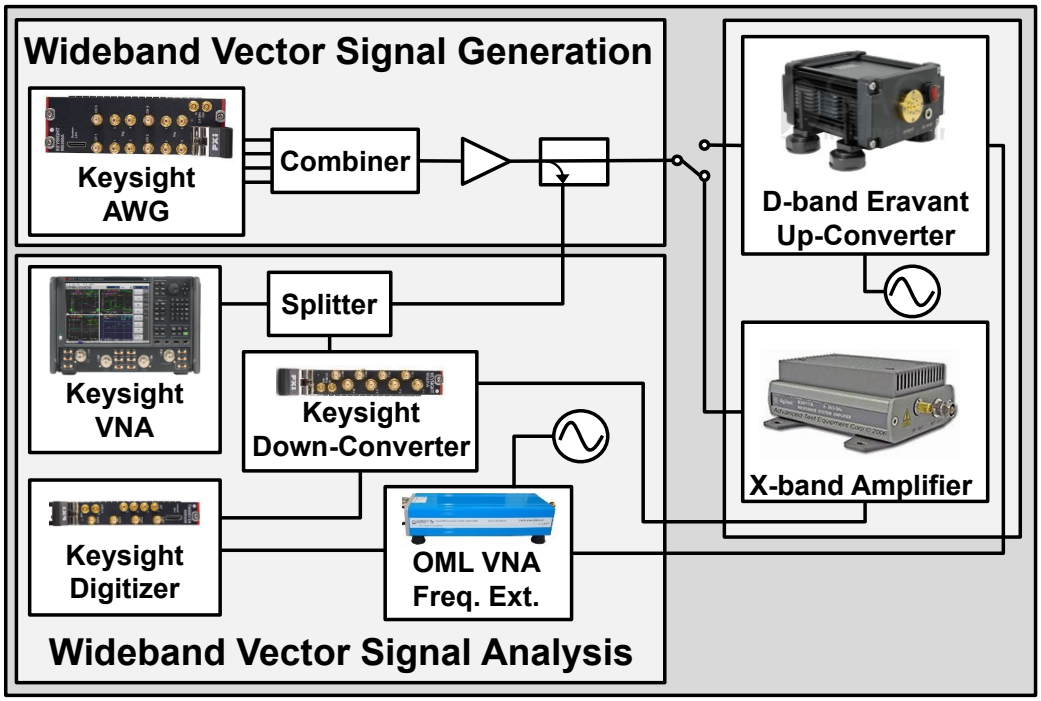


Figure 3.2: Measurement setup.

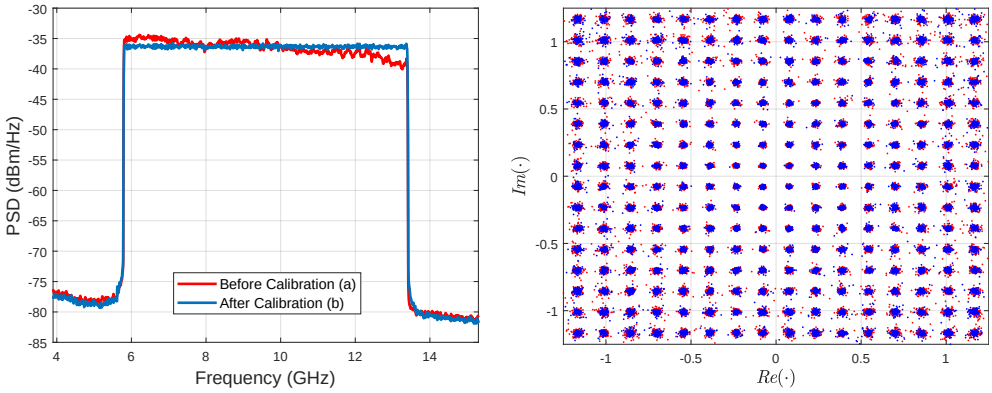


Figure 3.3: Measured PSD (Left) and constellation (Right) of a 256-QAM 8 GHz bandwidth OFDM signal centered at 9.6 GHz, generated using the proposed Method-1 with four RF-AWG channels: a) before transmitter calibration, and b) with the proposed calibration technique applied.

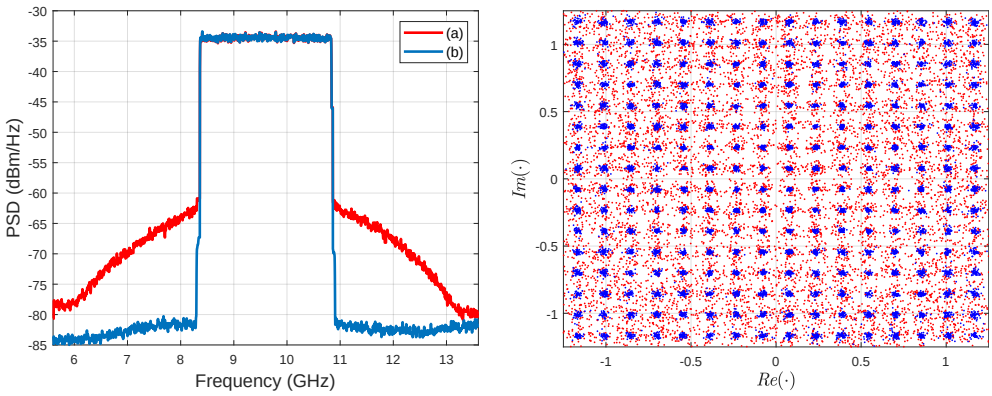


Figure 3.4: Measured PSD (Left) and constellation (Right) at an X-band amplified output driven with a 256-QAM 2.6 GHz bandwidth OFDM signal centered at 9.6 GHz, generated using the proposed Method-1 with four RF-AWG channels: a) before linearization applied; b) with linearization applied.

Next, measurement is done to evaluate the validity of the proposed Method-1 at D-band. Fig. 3.5 shows the PSD (Left) and constellation (Right) of a 256-QAM 4 GHz bandwidth OFDM signal centered at 129.6 GHz The signal was generated using Method-1 with two RF-AWG channels: a) before transmitter calibration; b) with transmitter calibration applied. The RNMSE and EVM improved from 27.1% and 3.6% before calibration in (a) to 3.3% and 3.2% with calibration applied in (b). Notably, the degradation in NMSE and EVM for D-band measurements is attributed to the up and down converter's LO phase noise.

Fig. 3.6 displays the PSD (Left) and constellation (Right) of a 256-QAM 7.6 GHz bandwidth OFDM signal centered at 9.6 GHz, generated using the proposed Method-2 with four RF-AWG channels: a) before transmitter calibration, and b) with transmitter calibration applied. The measurements demonstrate that the proposed real-time transmitter frequency-stitching method can generate excellent signals with calibration applied, where the reported NMSE and EVM after calibration improved from 86.7% and 1.85% before calibration in (a) to 0.39% and 0.37% with calibration applied in (b).

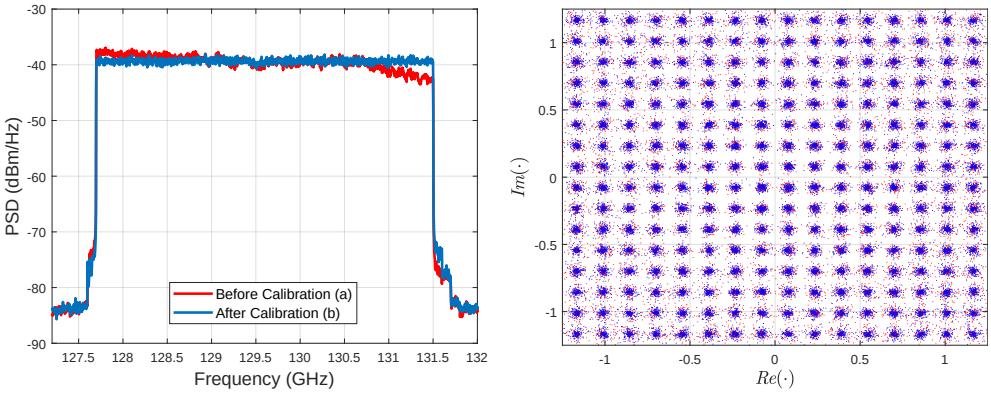


Figure 3.5: Measured PSD (Left) and constellation (Right) of a 256-QAM 4 GHz bandwidth OFDM signal centered at 129.6 GHz, generated using the proposed Method-1 with two RF-AWG channels: a) before transmitter calibration; b) with transmitter calibration applied.

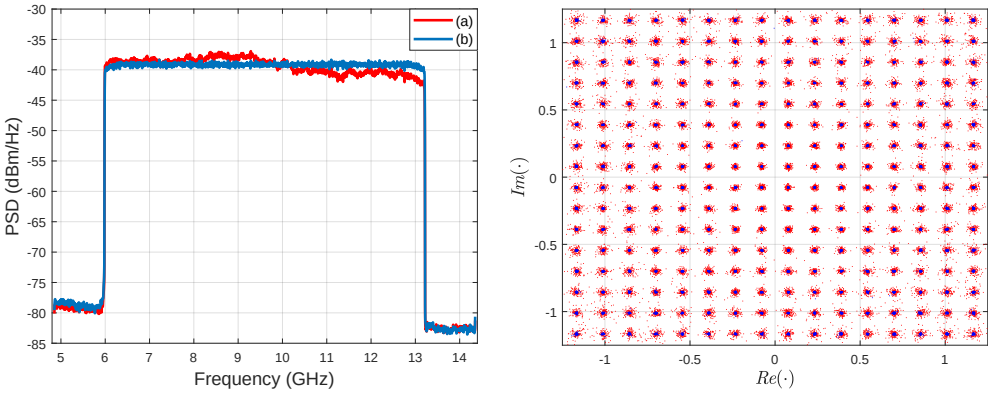


Figure 3.6: Measured PSD (Left) and constellation (Right) of a 256-QAM 7.6 GHz bandwidth OFDM signal centered at 9.6 GHz, generated using the proposed Method-2 with four RF-AWG channels: a) before transmitter calibration; b) with transmitter calibration applied.

3.3 Comparison with Other Wideband Signal Generation Methods

3.3.1 Measurement Setup

To demonstrate the different methods of generating wideband signals at D-Band, the measurement setup shown in Fig. 3.7 was developed. Three different signal sources representing the three signal generation methods discussed in previous section. The signal source for direct wideband IF generation was an 8-bit, 60 GHz bandwidth, and 128 Gsps AWG (M8199A from Keysight). The signal source for baseband signal generation + IQ mixer was a 12-bit, and 12 Gsps AWG (M8190A from Keysight) with 5 GHz bandwidth for both I and Q; the AWG baseband outputs are then fed to a IQ mixer (MMIQ-0626LSM from Marki Microwave) and the LO for the mixer is supplied from the VNA. The signal source for multiple AWG with channel bonding was a 14-bit, 2 GHz bandwidth, and 4.8 Gsps direct digital synthesis-based RF-AWG (M5300A from Keysight) with four synchronous phase-coherent channels. These signal sources generate signals at an IF of 9.6 GHz, the signal is then upconvertered to D-Band at 158.4 GHz using a WR6.5CCU from Virginia Diodes. The receiver consist of a D-Band downconverter (WR6.5CCD from Virginia Diodes), and a VNA (N5245B from Keysight). Note the that the LO for the D-Band up/downconverter is supplied from the VNA.

3.3.2 Measurement Results

The first set of measurement is a through test, connecting the three approaches directly to the receiver. Fig. 3.8 show the power spectral density (PSD) (Left) and constellation (Right) of a 256-QAM 8 GHz bandwidth OFDM signal centered at 158.4 GHz, with 120 KHz sub-carrier spacing, generated using equipment and method: a) M8199A; b) M8190A with IQ mixer; c) M5300A using channel bonding. The measured NMSE and EVM for M8199A is 1.8% and 1.5% in (a), compared to M8190A result 4.4% and 0.8% in (b), and M5300A result 1% and 1% in (c). From this measurement, the low speed RF-AWG method (M5300A) produced the best results, but this method requires extra signal processing step (i.e. channel bonding) to achieve the wide bandwidth. As shown in the spectrum of Fig. 3.8, the high speed RF-AWG (M8199A) is capable of generating very wide bandwidth signal, but it has much worse SNR compared to the other two method.

Next measurement compares the three signal generation methods for linearizing a D-Band amplifier using ILC, with 8 GHz linearization bandwidth. Fig. 3.9 show the PSD

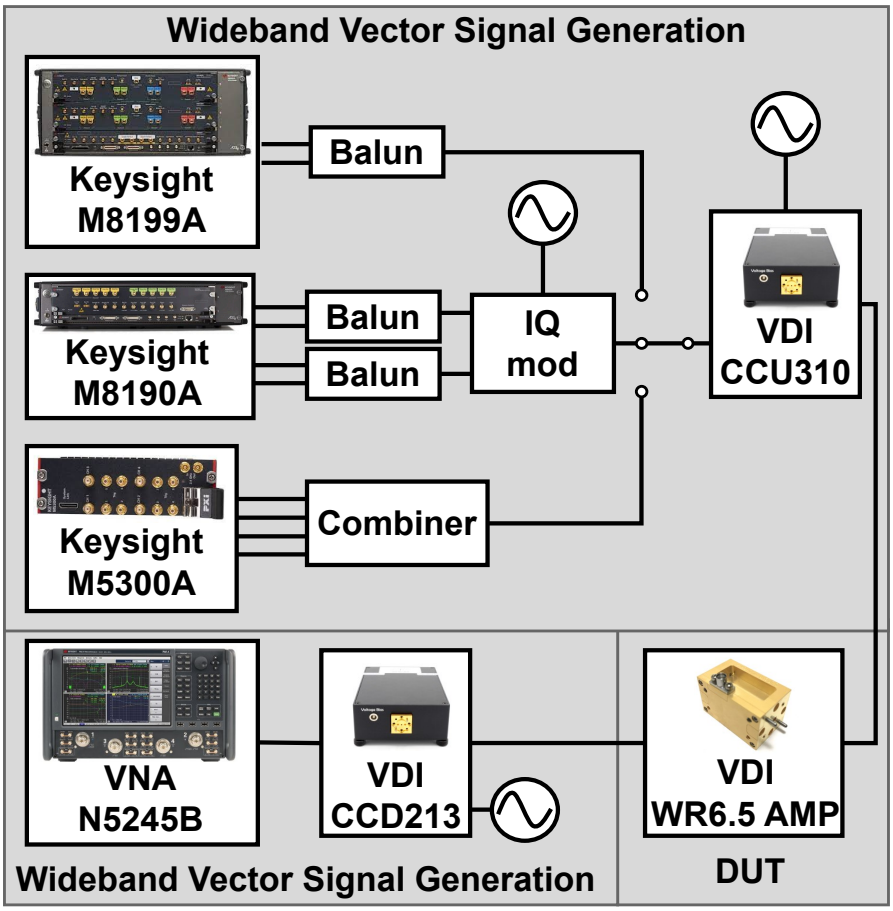


Figure 3.7: Block diagram of the measurement setup.

(Left) and constellation (Right) at a D-Band amplifier with a 256-QAM 2.6 GHz bandwidth OFDM signal centered at 158.4 GHz, with 120 KHz sub-carrier spacing: a) before linearization; b) M8199A; c) M8190A with IQ mixer; d) M5300A using channel bonding. The linearization method is ILC. The EVM and ACPR is 1% and -47.9/-50.7 dBc before the linearization in (a), and improved to 0.4% and -60.9/-63.8 dBc for M8190A in (c); 0.4% and -58.4/-62.4 dBc for M5300A in (d). The result of before and after linearization for M8199A is very similar, before linearization is 1% and -44.8/-47.1 dBc, to after linearization is 0.5% and -45.8/-49.1 dBc in (b). As shown in the spectrum of Fig. 3.9, the high speed RF-AWG (M8199A) has much worse SNR, the noise floor is above the non-linear distortion. This is due to the limited ENOB of the M8199A, not the method used for signal generation. Thus, this setup is not capable of linearizing the amplifier used in this

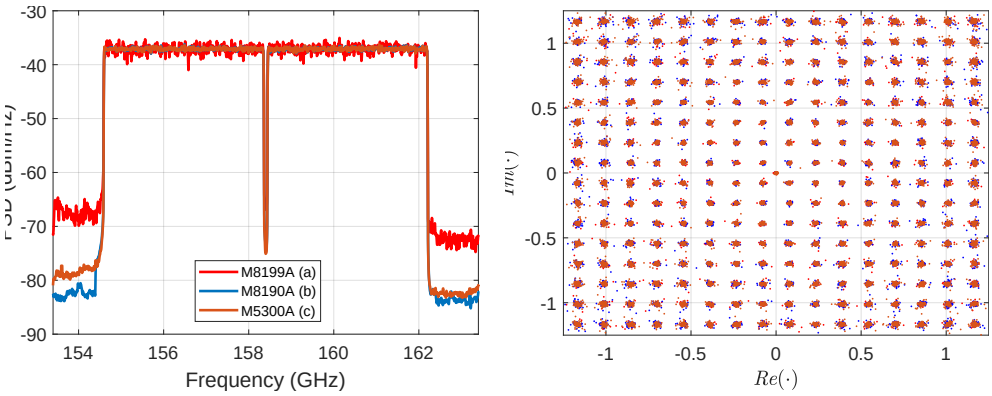


Figure 3.8: Measured PSD (Left) and constellation (Right) of a 256-QAM 8 GHz bandwidth OFDM signal centered at 158.4 GHz, through test, generating using equipment and method: a) M8199A; b) M8190A with IQ mixer; c) M5300A using channel bonding.

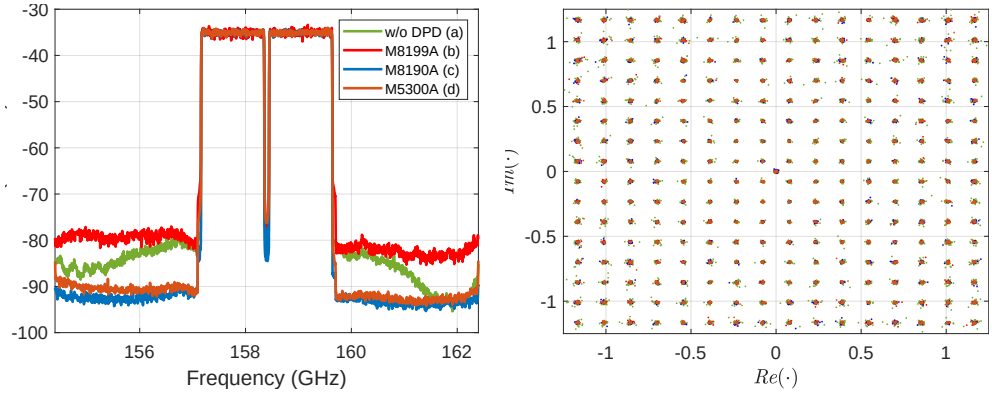


Figure 3.9: Measured PSD (Left) and constellation (Right) at a D-Band amplifier of a 256-QAM 2.6 GHz bandwidth OFDM signal centered at 158.4 GHz, linearizing with ILC: a) before linearization; and after linearization for the three signal generation approaches: b) M8199A; c) M8190A with IQ mixer; d) M5300A using channel bonding.

measurement at this compression level, unless an AWG with higher ENOB and acceptable bandwidth would be available. As for the other two signal generation approaches, the excellent SNR performance, due to the high resolution of the AWGs used, are suitable for performing component testing.

3.4 Conclusion

In this chapter, two wideband signal generation method are proposed. The first method leverages test signal periodicity, enabling wideband signal partitioning into sub-bands. The second approach, tailored for real-time applications, utilizes OFDM signal characteristics for partitioning at the OFDM symbol level. Additionally, a frequency calibration technique addressed nonidealities in the transmitter's RF front-end during frequency-stitching-based signal generation. Experimental validations at X-band and D-band showcased outstanding signal quality of the proposed methods, achieving low EVMs of 0.3% when generating a 7.2 GHz 256-QAM OFDM signal and supporting modulation bandwidths up to 8 GHz. A comparison experiment between three different architectures that showed the proposed wideband signal generation method performance against using IQ DAC and IQ mixer signal generation and using high speed low resolution DAC signal generation. The experiment results show the proposed frequency stitching method and the IQ DAC and IQ mixer architecture outperforms the high speed DAC signal generation method by obtaining better ACPR in component testing, achieving -60.9/-63.8 dBc and -58.4/-62.4 dBc, respectively, while the high speed DAC signal generation method achieved an ACPR of -45.8/-49.1 dBc.

Chapter 4

Frequency Stitching Applied to IQ DAC and IQ Mixer Signal Generation Architecture

This chapter discusses the contribution from **Publication III**. This chapter presents the frequency stitching methods for signal generation applied in multiple IQ DACs and IQ mixers architectures, along with a corresponding calibration method for this architecture. The comparison measurements in Chapter 3 demonstrated that the IQ DACs and IQ mixer architecture can achieve high signal quality when generating wideband signals. By applying frequency stitching to multiple IQ DACs and IQ mixers, it becomes possible to achieve even wider bandwidths while maintaining high signal quality.

Compared to RF DAC architectures, the IQ DAC and IQ mixer architecture offer greater scalability. The signal bandwidth in RF DACs is constrained by the maximum frequency the DAC can support. In contrast, the IQ DAC and IQ mixer architecture generates the signal at baseband and then upconverts it to RF, allowing for more flexible bandwidth scaling. However, this architecture comes with certain disadvantages, such as the presence of IQ imbalance, which necessitates a more complex calibration process.

The proposed architecture and calibration method are validated through measurements, where wideband signals are generated using the IQ DACs and IQ mixer architecture. The results demonstrate the effectiveness of the frequency-stitching approach in extending signal bandwidth while maintaining signal quality.

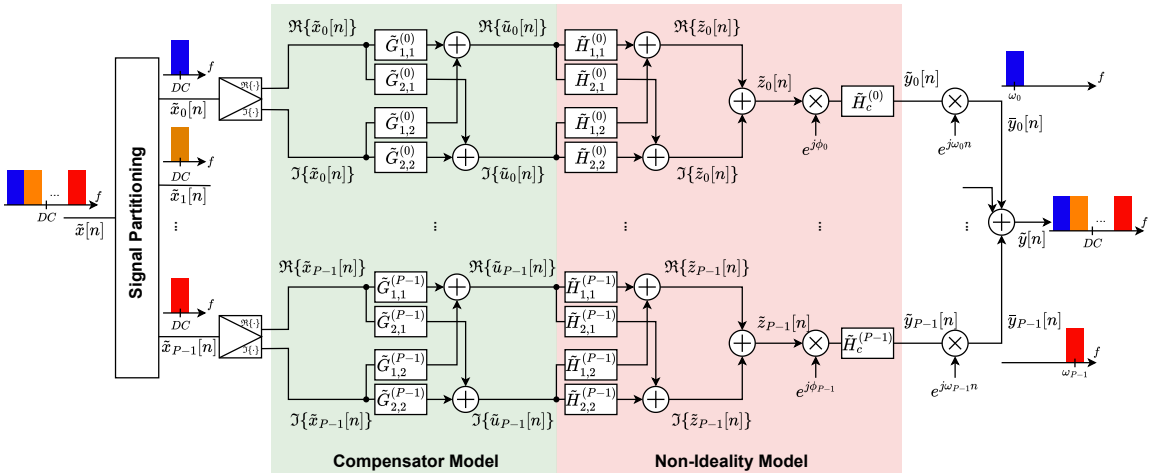


Figure 4.1: Equivalent complex baseband representation of the proposed frequency-stitching ultra-wideband signal generator, illustrating non-idealities and calibration filters.

4.1 Calibration Formulation

When generating the different signal portions, $\tilde{x}_p[n]$, in practice, the proposed scheme encounters several non-idealities as shown in Fig. 4.1. These non-idealities arise from IQ imbalance introduced by the mixers, phase offsets due to LOs, and varying frequency responses across the transmitter chains and combiner network. To address these issues, a calibration method is required, which is presented in this subsection.

For notational convenience, the following derivation is presented in the discrete-time complex baseband domain (refer to Fig. 4.1). This simplifies the representation and analysis of non-idealities within the system. Figure 4.1 illustrates the modeled non-idealities. The complex transfer functions $\tilde{H}_{1,1}^{(p)}$, $\tilde{H}_{1,2}^{(p)}$, $\tilde{H}_{2,1}^{(p)}$, and $\tilde{H}_{2,2}^{(p)}$ represent the frequency responses of the IQ imbalance model filters for the p-th channel. These filters account for imperfections in the IQ mixers that can cause gain and phase imbalances between the I and Q components of the signal. Additionally, the complex transfer function $\tilde{H}_c^{(p)}$ represents the non-ideality model filter's frequency response introduced by the transmitter RF components and the combiner network in the p-th channel. This filter captures the combined effects of various linear impairments within the transmitter chain, such as phase and gain errors in amplifiers, filters, and the combiner network. Let $\tilde{z}_p[n]$ represent the non-ideal signal at the p-th transmitter channel after mixing and before combining. Assuming that the calibration is not applied, such that $\tilde{u}_{(p)}[n] = \tilde{x}_{(p)}[n]$, the signal $\tilde{z}_{(p)}[n]$ can be expressed as a function of

the mixer's non-idealities as follows:

$$\begin{aligned}\tilde{z}_p[n] =&\Re\{\tilde{x}_p[n]\} \circledast \tilde{h}_{1,1}^{(p)}[n] + \Im\{\tilde{x}_p[n]\} \circledast \tilde{h}_{1,2}^{(p)}[n] \\ &+ j\Im\{\tilde{x}_p[n]\} \circledast \tilde{h}_{2,2}^{(p)}[n] + j\Re\{\tilde{x}_p[n]\} \circledast \tilde{h}_{2,1}^{(p)}[n],\end{aligned} \tag{4.1}$$

where $\Re\{\cdot\}$ and $\Im\{\cdot\}$ are the real and imaginary operations, and $\tilde{h}_{\ell,m}^{(p)}[n]$ is the impulse response of $\tilde{H}_{\ell,m}^{(p)}(\omega)$. At the combiner output, the combined signal $\tilde{y}[n]$ can be expressed as follows:

$$\tilde{y}[n] = \sum_{p=0}^{P-1} \bar{y}_p[n], \tag{4.2}$$

where,

$$\bar{y}_p[n] = (\tilde{z}_p[n] \circledast \tilde{h}_c^{(p)}[n])e^{j\phi_p}e^{j\omega_p n}, \tag{4.3}$$

$\tilde{h}_c^{(p)}[n]$ is the impulse response of $\tilde{H}_c^{(p)}(\omega)$, and ϕ_p is the relative phase offset experienced by the p-th transmitter channel. Alternatively, (4.2) can be rewritten where the combiner network non-ideal response and the phase offset between the different branches are absorbed with the IQ imbalance filters, such that:

$$\tilde{y}[n] = \sum_{p=0}^{P-1} \tilde{y}_p[n]e^{j\omega_p n}, \tag{4.4}$$

where,

$$\tilde{y}_p[n] = (\tilde{z}_p[n] \circledast \tilde{h}_c^{(p)}[n])e^{j\phi_p}. \tag{4.5}$$

Substituting, (4.1) in (4.5), we then have:

$$\begin{aligned}\tilde{y}_p[n] =&\Re\{\tilde{x}_p[n]\} \circledast \tilde{h}_{1,1}^{\prime(p)}[n] + \Im\{\tilde{x}_p[n]\} \circledast \tilde{h}_{1,2}^{\prime(p)}[n] \\ &+ j\Im\{\tilde{x}_p[n]\} \circledast \tilde{h}_{2,2}^{\prime(p)}[n] + j\Re\{\tilde{x}_p[n]\} \circledast \tilde{h}_{2,1}^{\prime(p)}[n],\end{aligned} \tag{4.6}$$

where the impulse responses $\tilde{h}_{1,1}^{\prime(p)}[n]$, $\tilde{h}_{1,2}^{\prime(p)}[n]$, $\tilde{h}_{2,1}^{\prime(p)}[n]$, and $\tilde{h}_{2,2}^{\prime(p)}[n]$ model the combined non-idealities experienced in the p-th channel, and are defined as follows:

$$\tilde{h}_{\ell,m}^{\prime(p)}[n] = (\tilde{h}_{\ell,m}^{(p)}[n] \circledast \tilde{h}_c^{(p)}[n])e^{j\phi_p}. \tag{4.7}$$

To compensate for the non-idealities described in (4.6), this work employs multi-tone signals. Fig. 4.2 shows a block diagram of the proposed calibration scheme for the special case of two transmitters (i.e., $P = 2$). Specifically, each transmitter channel is assigned a signal, $\tilde{u}_p[n] = \tilde{u}_I^{(p)}[n] + j\tilde{u}_Q^{(p)}[n]$. The signals $\tilde{u}_I^{(p)}[n]$ and $\tilde{u}_Q^{(p)}[n]$ are real interleaved multi-tone calibration signals, with their respective tones selected to avoid occupying the same frequency grid. Let $\tilde{U}_I^{(p)}(\omega)$ and $\tilde{U}_Q^{(p)}(\omega)$ denote the Fourier transforms of $\tilde{u}_I^{(p)}[n]$ and $\tilde{u}_Q^{(p)}[n]$, respectively. We define Ω_p^- and Ω_p^+ to be the set of uniformly spaced negative and positive frequency points, respectively, with spacing Δf, such that:

$$\Omega_p^- = \{\ell\Delta f - f_{\text{offset}}^{(p)} \mid \ell \in \mathbb{Z}, \ell < 0\}, \tag{4.8}$$

$$\Omega_p^+ = \{\ell\Delta f + f_{\text{offset}}^{(p)} \mid \ell \in \mathbb{Z}, \ell \geq 0\}, \tag{4.9}$$

and $f_{\text{offset}}^{(p)}$ is a frequency offset corresponding assigned to the p-th channel calibration signal starting tone. Furthermore, we define $\Omega_I^{(p)}$ and $\Omega_Q^{(p)}$ to be the even and odd entries of the set $\Omega_p = \Omega_p^- \cup \Omega_p^+$, respectively. The signal $\tilde{U}_I^{(p)}(\omega)$ is constructed such that $\tilde{U}_I^{(p)}(\omega_I^{(p)}) \neq 0$ for $\omega_I^{(p)} \in \Omega_I^{(p)}$ and $\tilde{U}_I^{(p)}(\omega_Q^{(p)}) = 0$ for $\omega_Q^{(p)} \in \Omega_Q^{(p)}$. Similarly, $\tilde{U}_Q^{(p)}(\omega)$ is constructed such that $\tilde{U}_Q^{(p)}(\omega_Q^{(p)}) \neq 0$ for $\omega_Q^{(p)} \in \Omega_Q^{(p)}$ and $\tilde{U}_Q^{(p)}(\omega_I^{(p)}) = 0$ for $\omega_I^{(p)} \in \Omega_I^{(p)}$. This ensures that the tones in $\tilde{u}_I^{(p)}[n]$ and $\tilde{u}_Q^{(p)}[n]$ do not interfere with each other, facilitating accurate compensation for the non-idealities in the system. During the calibration stage, the signal $\tilde{y}_p[n]$ can be expressed in the frequency domain as a function of $\tilde{U}_I^{(p)}(\omega)$ and $\tilde{U}_Q^{(p)}(\omega)$ as follows:

$$\begin{bmatrix} \tilde{Y}_I^{(p)}(\omega) \\ \tilde{Y}_Q^{(p)}(\omega) \end{bmatrix} = \begin{bmatrix} \tilde{H}_{1,1}^{\prime(p)}(\omega), \tilde{H}_{1,2}^{\prime(p)}(\omega) \\ \tilde{H}_{2,1}^{\prime(p)}(\omega), \tilde{H}_{2,2}^{\prime(p)}(\omega) \end{bmatrix} \begin{bmatrix} \tilde{U}_I^{(p)}(\omega) \\ \tilde{U}_Q^{(p)}(\omega) \end{bmatrix}, \tag{4.10}$$

where $\tilde{Y}_I^{(p)}(\omega)$ and $\tilde{Y}_Q^{(p)}(\omega)$ are the Fourier transform of $\Re\{\tilde{y}_p[n]\}$ and $\Im\{\tilde{y}_p[n]\}$, respectively.

The IQ imbalance in different branches causes tones to appear in each other's frequency grid, as shown in Fig. 4.2. Since the tones lie on an interleaved frequency grid, the leaked in-phase and quadrature tones are easily identified from $\tilde{y}_p[n]$. This enables the extraction of the forward models $\tilde{H}_{1,1}^{\prime(p)}(\omega)$, $\tilde{H}_{1,2}^{\prime(p)}(\omega)$, $\tilde{H}_{2,1}^{\prime(p)}(\omega)$, and $\tilde{H}_{2,2}^{\prime(p)}(\omega)$ in a single capture. The frequency-domain forward model extraction for the four filters in the p-th channel is achieved using $\tilde{Y}_I^{(p)}(\omega)$ and $\tilde{Y}_Q^{(p)}(\omega)$, along the calibration signals $\tilde{U}_I^{(p)}(\omega)$ and $\tilde{U}_Q^{(p)}(\omega)$. Using $\tilde{Y}_I^{(p)}(\omega)$, the forward model $\tilde{H}_{1,1}^{\prime(p)}(\omega_I^{(p)})$ is identified by computing the transfer function relating the input tones on the $\omega_I^{(p)} \in \Omega_I^{(p)}$ frequency grid, $\tilde{U}_I^{(p)}(\omega_I^{(p)})$, and the tones on the $\omega_I^{(p)}$ frequency grid in $\tilde{Y}_I^{(p)}(\omega)$. Additionally, the IQ imbalance filter $\tilde{H}_{1,2}^{\prime(p)}(\omega_Q^{(p)})$,

which causes the Q tones to appear in $\tilde{Y}_I^{(p)}(\omega)$, is computed using the input tones on the $\omega_Q^{(p)} \in \Omega_Q^{(p)}$ frequency grid, $\tilde{U}_Q^{(p)}(\omega_Q^{(p)})$, and the corresponding tones in the output signal $\tilde{Y}_I^{(p)}(\omega)$. Accordingly, we have:

$$\tilde{H}_{1,1}^{\prime(p)}(\omega_I^{(p)}) = \frac{\tilde{Y}_I^{(p)}(\omega_I^{(p)})}{\tilde{U}_I^{(p)}(\omega_I^{(p)})}, \tag{4.11}$$

and

$$\tilde{H}_{1,2}^{\prime(p)}(\omega_Q^{(p)}) = \frac{\tilde{Y}_I^{(p)}(\omega_Q^{(p)})}{\tilde{U}_Q^{(p)}(\omega_Q^{(p)})}. \tag{4.12}$$

Similarly, using $\tilde{Y}_Q^{(p)}(\omega)$, the forward models $\tilde{H}_{2,2}^{\prime(p)}(\omega_Q^{(p)})$ and $\tilde{H}_{2,2}^{\prime(p)}(\omega_I^{(p)})$ can be extracted as follows:

$$\tilde{H}_{2,2}^{\prime(p)}(\omega_Q^{(p)}) = \frac{\tilde{Y}_Q^{(p)}(\omega_Q^{(p)})}{\tilde{U}_Q^{(p)}(\omega_Q^{(p)})}, \tag{4.13}$$

and

$$\tilde{H}_{2,1}^{\prime(p)}(\omega_I^{(p)}) = \frac{\tilde{Y}_Q^{(p)}(\omega_I^{(p)})}{\tilde{U}_I^{(p)}(\omega_I^{(p)})}. \tag{4.14}$$

Since the $\Omega_I^{(p)}$ and $\Omega_Q^{(p)}$ frequency grids are offset, frequency grid alignment is necessary for the four forward models. This alignment can be achieved using frequency interpolation to obtain $\tilde{H}_{1,1}^{\prime(p)}(\omega)$, $\tilde{H}_{1,2}^{\prime(p)}(\omega)$, $\tilde{H}_{2,1}^{\prime(p)}(\omega)$, and $\tilde{H}_{2,2}^{\prime(p)}(\omega)$ from $\tilde{H}_{1,1}^{\prime(p)}(\omega_I^{(p)})$, $\tilde{H}_{1,2}^{\prime(p)}(\omega_Q^{(p)})$, $\tilde{H}_{2,1}^{\prime(p)}(\omega_I^{(p)})$, and $\tilde{H}_{2,2}^{\prime(p)}(\omega_Q^{(p)})$, respectively. Once the forward models are estimated, the inverse compensation model $\tilde{\mathbf{G}}'(\omega)$ can be obtained as follows:

$$\tilde{\mathbf{G}}'(\omega) = \begin{bmatrix} H_{1,1}^{\prime(p)}(\omega), H_{1,2}^{\prime(p)}(\omega) \\ H_{2,1}^{\prime(p)}(\omega), H_{2,2}^{\prime(p)}(\omega) \end{bmatrix}^{-1} = \begin{bmatrix} G_{1,1}^{(p)}(\omega), G_{1,2}^{(p)}(\omega) \\ G_{2,1}^{(p)}(\omega), G_{2,2}^{(p)}(\omega) \end{bmatrix}, \tag{4.15}$$

where $G_{1,1}^{(p)}(\omega)$, $G_{1,2}^{(p)}(\omega)$, $G_{2,1}^{(p)}(\omega)$, and $G_{2,2}^{(p)}(\omega)$ are the calibration filters' frequency responses corresponding to the p-th transmitter channel.

In the above formulation, it is assumed that the signal $\tilde{y}_p[n]$ can be directly measured. However, in practice, calibration needs to be performed using the actual signal available at the combiner output $\tilde{y}[n]$. To that end, one approach involves sequentially enabling each transmitter channel, measuring the resulting signal $\bar{y}_p[n]$ at the combiner output, and then downconverting the signal to baseband to obtain $\tilde{y}_p[n]$. While seemingly straightforward, this approach suffers from increased calibration time and is unable to compensate for the

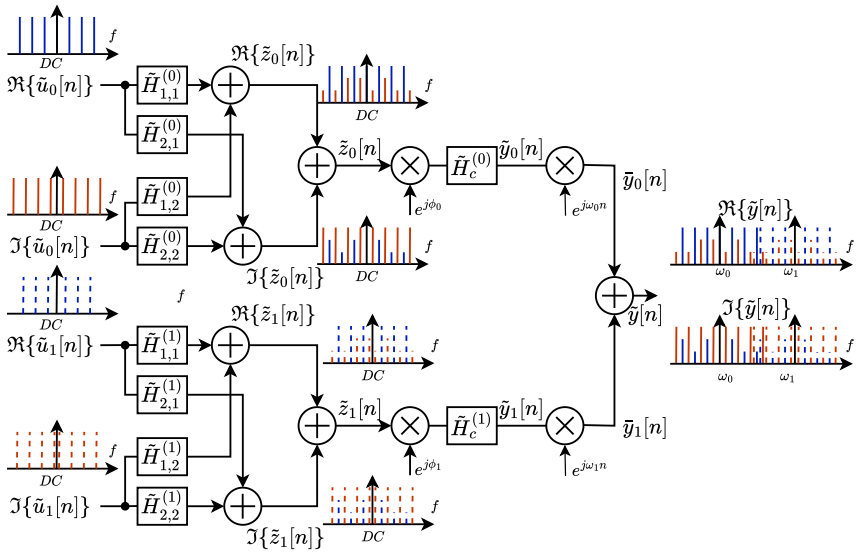


Figure 4.2: Conceptual diagram of the effects of IQ imbalance on the generated signal in a two-channel frequency-stitching signal generator (i.e., $P = 2$). The figure also showcases the proposed non-uniformly interleaved calibration signal.

relative phase offsets between different transmitter channels, ϕ_p. Therefore, performing the calibration of all transmitter channels simultaneously is highly desirable. However, simultaneous calibration introduces a new challenge: during simultaneous calibration, the edge tones of the calibration signals from different channels should not overlap when combined at RF to prevent inter-channel interference. Conversely, if the edge tones are entirely non-overlapping, achieving frequency response continuity across channels, which is essential for accurate signal reconstruction, becomes difficult. To mitigate this problem, the calibration signals from two adjacent channels are designed such that their respective edge frequency tones are interleaved, as shown in Fig. 4.2. This approach results in the generation of a non-uniformly spaced multi-tone signal at the transmitter combined output.

Let $\mathrm{BW}^{(p)}_{\mathrm{cal}}$ denote the bandwidth of the p-th calibration signal, $\tilde{u}_p[n]$. To ensure that the different multi-tone calibration signals in the different frequency channels have their edge frequency tones interleaved, $\mathrm{BW}^{(p)}_{\mathrm{cal}}$ has to be larger than $\frac{\mathrm{BW}_{\mathrm{stitching}}}{P}$. Furthermore, $\mathrm{BW}^{(p)}_{\mathrm{cal}}$ cannot exceed the maximum bandwidth that each channel can generate, referred to $\mathrm{BW}_{\mathrm{AWG}}$. Therefore, the following inequality must be satisfied:

$$\mathrm{BW}_{\mathrm{AWG}} \geq \mathrm{BW}^{(p)}_{\mathrm{cal}} > \frac{\mathrm{BW}_{\mathrm{stitching}}}{P}, \tag{4.16}$$

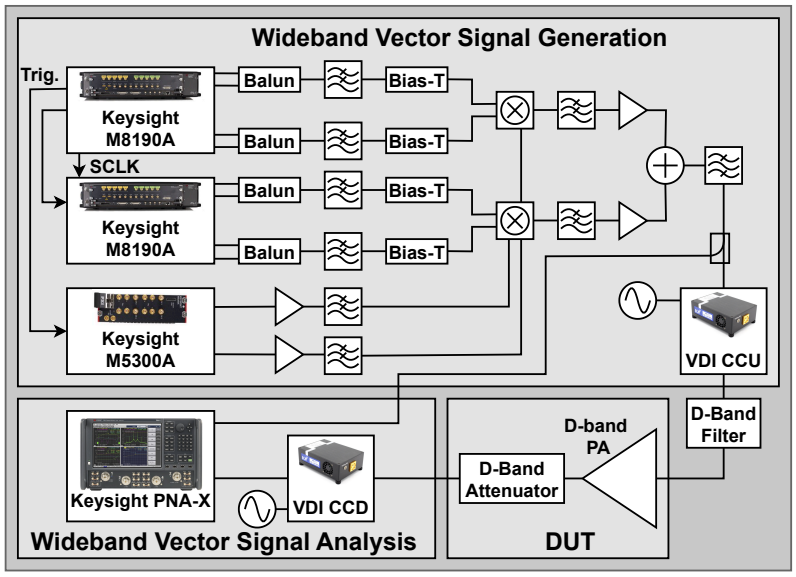


Figure 4.3: Block diagram of the D-band measurement setup used to validate the proposed frequency-stitching based signal generation method.

Furthermore, to avoid overlapping of the edge frequency tones of different calibration signals in the RF domain, the following requirement must be satisfied:

$$\frac{\mathrm{BW}_{\mathrm{cal}}^{(\ell+1)} + \mathrm{BW}_{\mathrm{cal}}^{(\ell)}}{2} - \frac{\mathrm{BW}_{\mathrm{stitching}}}{P} \neq \alpha \Delta f, \tag{4.17}$$

where α is an arbitrarily chosen integer and $\ell \in \{0, 2, ...P-2\}$.

4.2 Experimental Validation

4.2.1 Measurement Setup

This section presents the experimental validation of the proposed signal generation method at D-band. The measurement setup, as shown in Fig. 4.3, was developed for this purpose.

The baseband modulated signals used in the experiments are generated by two 12-bit, 12 Gsps AWGs (model M8190A, Keysight Technologies). Each AWG generates both in-phase (I) and quadrature (Q) signals. The two AWGs are synchronized, with one designated as the primary unit providing the sampling clock and trigger signal for the other

(secondary) AWG. The baseband I/Q signals from the AWGs are then upconverted to distinct IFs using two IQ modulators (Marki Microwave MLIQ0416L). The LOs driving these modulators are generated by digital sources (Keysight M5300A) featuring four synchronous and phase-coherent channels. These LO signals are amplified using driver amplifiers (Macom MAAM-011109) and passed through lowpass filters (Marki Microwave FLP1250) for conditioning. The amplification ensures sufficient power for the IQ modulators, while the filtering minimizes unwanted spectral components (spurious signals) in the LOs. To guarantee phase coherence between the AWGs and the LOs, a synchronization trigger signal from the primary AWG is provided to the LO equipment.

The resulting IF signals from the IQ mixer outputs are further processed. Each IF signal is filtered by a dedicated low pass filter (Mini-Circuit ZLFV-K1652+) and amplified by a driver amplifier (Mini-Circuit ZVA-203GX+). Finally, the two IF signals are combined using a Wilkinson power combiner (Marki Microwave PD0140). The combined output is then filtered by a bandpass filter (Mini-Circuit ZBSS-12G-S+) for additional signal conditioning before being fed into a D-band upconverter (VDI WR6.5CCU) through a directional coupler (Krytar Directional Couplers 1851). For the receiver setup, a D-band downconverter (VDI WR6.5CCD) is used to downconvert the D-band signal back to the IF frequency. The downconverted IF and the directional coupler coupled port are routed to a vector network analyzer (VNA) (Keysight N5245B) operating in spectrum analysis mode. The LOs for the D-band up and downconverters are provided by the VNA.

The measurements are performed using OFDM signals with modulation bandwidths of 4 GHz and 12 GHz. The sub-carriers were modulated using 256-QAM and spaced by 120 kHz. Furthermore, a total number of data sub-carriers K_{D} of 31680 and 95040, and fast Fourier transform sizes K_{FFT} of 40950 and 122850 were used for the 4 GHz and 12 GHz modulation bandwidth settings, respectively. The used test signals are characterized by a peak-to-average power ratio (after crest factor reduction using clipping and filtering) of 10 dB. The 4 GHz and 12 GHz test signals are complex sampled at 12 Gsps. Due to hardware limitations, the generated test signal sub-carriers positioned around the DC of each sub-band (approximately $\pm$7.5 MHz) are nulled. This is a consequence of the proposed measurement validation setup utilizing differential DACs and bias-tees for LO cancellation, which inhibits the generation of modulated signals near the DC of each sub-band. As a result, sub-carriers in proximity to the DC of each sub-band have been intentionally zeroed to prevent distortion.

In the reported results, the stitching bandwidth, $\mathrm{BW}_{\mathrm{stitching}}$, was set to 12 GHz, and the number of partitions (sub-bands), P, was set to two. For the calibration process, multi-tone signals were used with the following configuration: the I and Q tones were interleaved with an offset of 1 MHz, and the spacing between tones was set to 2 MHz. The calibration

bandwidths were set to $\mathrm{BW}_{\mathrm{cal}}^{(0)} = 6.02$ GHz and $\mathrm{BW}_{\mathrm{cal}}^{(1)} = 6.02$ GHz for the first and second channels, respectively. Additionally, the frequency offsets were set to $f_{\mathrm{offset}}^{(0)} = 1$ MHz and (for channel one) and $f_{\mathrm{offset}}^{(1)} = 0.5$ MHz (for the second channel). These settings satisfy the conditions in Equations (4.16) and (4.17), ensuring interleaved edge tones without overlap in the RF domain and achieving the desired non-uniformly spaced multi-tone signal at the combiner output.

4.2.2 Measurement Results

Fig. 4.4 and Fig. 4.5 show the measured power spectrum density (PSD) and constellation at D-band of a 256-QAM 12 GHz bandwidth OFDM signal generated using the proposed method: a) before calibration, and b) with the proposed calibration applied. These measurements were performed with the combined IF signal centered at 11 GHz and the D-band output set to 149 GHz. The IQ mixers' outputs were centered around 8 GHz and 14 GHz, respectively. As evident from Fig. 4.4, the proposed calibration method is able to significantly improve the generated signal quality, where the NMSE and EVM reduced from 82.6% and 23.8% before calibration in Fig. 4.4 (a) to 2% and 1% after calibration Fig. 4.4 (b). The low NMSE after calibration highlights the effectiveness of the proposed scheme in correcting for magnitude and phase offsets between the different transmitter channels. It also addresses the IQ imbalance introduced by the IQ mixers.

Fig. 4.6 shows the measured PSD of the error signal, defined as $\tilde{e}[n] = \tilde{y}[n] - \tilde{x}[n]$, before and after calibration. These error signals correspond to the data presented in Fig. 4.4. After calibration (Fig. 4.6 (b)), the error signal's PSD becomes uniformly distributed across the frequency range. This indicates that the proposed calibration using non-uniform interleaved tones effectively avoids discontinuities in the frequency responses around DC. These discontinuities were previously pronounced in the error PSD plot before calibration in Fig. 4.6 (a).

To validate the applicability of the proposed method for testing components at D-band frequencies, a D-band PA operated in its non-linear regime serves as the DUT. The D-band upconverter output feeds the PA with the PA output connected to a waveguide attenuator and then to a downconver. The test signal has a bandwidth of 4 GHz bandwidth with sub-carriers modulated using 256-QAM. Both the linearization and stitching bandwidths are set to 12 GHz. Fig. 4.7 shows the PSD of the measured 256-QAM 4 GHz OFDM signal at D-band, before and after calibration and with the PA bypassed. Before Calibration, the measured signal exhibits an adjacent channel power ratio (ACPR) of -19.2/-21.1 dBc and an NMSE of 47.2%. After Calibration, the proposed calibration scheme significantly improves

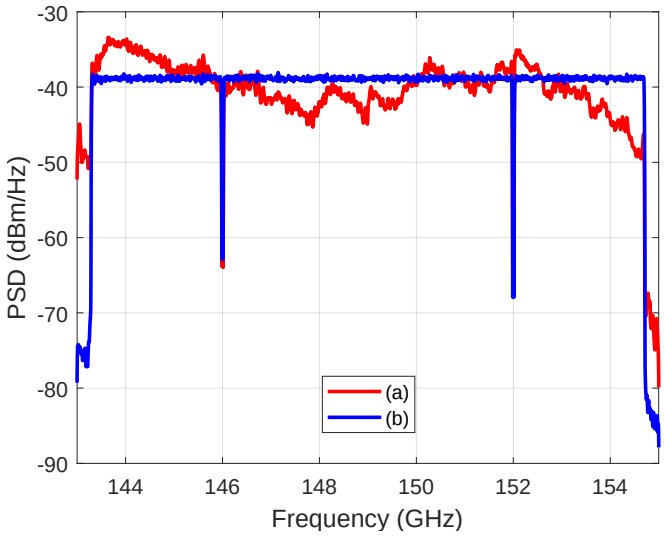


Figure 4.4: Measured PSD at D-band of a 256-QAM 12 GHz bandwidth OFDM signal generated using the proposed method: a) before calibration, and b) with the proposed calibration applied.

the signal quality. The ACPR is reduced to -43/-43.1 dB, the NMSE is lowered to 1.3%, and the EVM is 0.9%. The poor ACPR measurement before calibration is attributed to the image signal arising from IQ imbalance. The calibration effectively mitigates this issue, achieving ACPR performance limited only by the source noise floor. These measurements establish a baseline for the transmitter's SNR and the maximum achievable linearization ACPR when linearizing the PA. Ultimately, this maximum ACPR is limited by the source SNR, which is approximately -43/-43.1 dB in this case.

Fig. 4.8 and Fig. 4.9 illustrate the measured PSD and constellation diagrams at the D-band PA output when driven with a 4 GHz bandwidth, 256-QAM OFDM signal before and after linearization. The results show significant improvement in both ACPR and EVM after linearization. Before linearization (with calibration applied), the ACPR measured -27.8/-26 dBc and the EVM was 8.5%. After linearization (with calibration applied), the ACPR improved to -42.8/-43.1 dBc and the EVM dropped to 1.2%. Moreover, the application of the linearization technique successfully restored the distorted signal constellation at the PA output, as depicted in Fig. 4.9 (b).

Fig. 4.10 and Fig. 4.11 depict the gain and phase distortion plots measured at the D-band PA output before and after linearization. From Fig. 4.10 and Fig. 4.11, it is clear that the PA was able to be linearized and the memory effects exhibited by the PA were

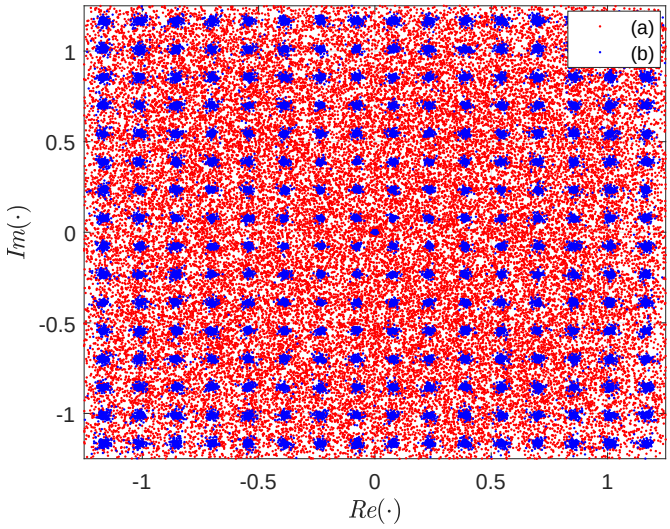


Figure 4.5: Measurend constellation at D-band of a 256-QAM 12 GHz bandwidth OFDM signal generated using the proposed method: a) before calibration, and b) with the proposed calibration applied.

considerably reduced. Interestingly, the ACPR at the DUT output after linearization (-42.8/-43.1 dBc) matches the best ACPR achievable by the source. This suggests the DUT has been linearized to the source's noise floor. These measurements validate the effectiveness of the proposed signal generation and calibration method for component testing at D-band frequencies.

4.3 Conclusion

In this chapter, the proposed frequency stitching signal generation methods are applied to IQ DACs and IQ mixers architecture to achieve wider bandwidth. A novel calibration technique is developed to address the IQ imbalance from using this architecture, and distortion from other components in the setup. This calibration technique uses non-uniform and interleaved tones to calibrates all the IQ DAC and IQ mixer paths simultaneously to ensure the phase offset between paths are accounted for. Experimental validation at D-band frequencies (around 149 GHz) demonstrated the successful generation of 256-QAM OFDM signals with an instantaneous bandwidth of up to 12 GHz and a peak data rate of 96 Gbps. Notably, proof-of-concept validation was achieved using two IQ-DACs and two IQ mixers. The calibration technique significantly improved the EVM and NMSE, reducing them from

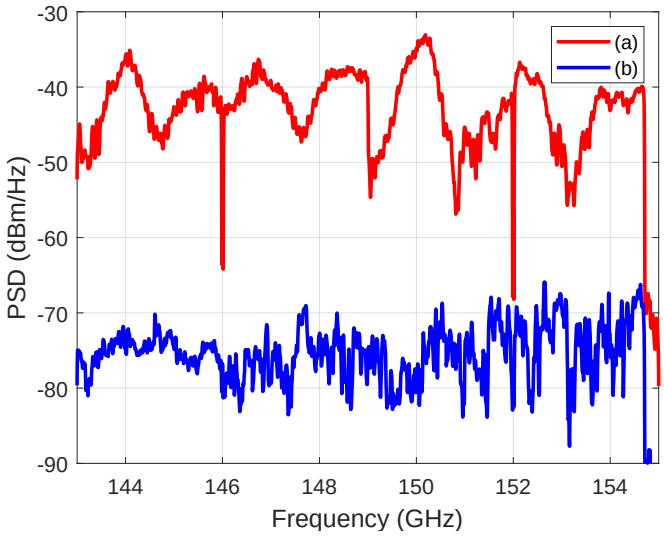


Figure 4.6: Measured PSD of the error signal at D-band of a 256-QAM 12 GHz bandwidth OFDM signal generated using the proposed method: a) before calibration, and b) with the proposed calibration applied.

82.6% and 23.8% to less than 2% and 1%, respectively, for a 12 GHz bandwidth 256-QAM OFDM signal. The approach's suitability for component testing was further validated by linearizing a D-band amplifier operating in its non-linear region, driven by a 4 GHz 256-QAM OFDM signal. The linearization improved the adjacent channel power ratio (ACPR) from -27.8/-26 dBc to -42.8/-43.1dBc and reduced the EVM from 8.5% to 1.2%, ensuring a linearization bandwidth over 12 GHz. These results highlight the effectiveness and versatility of the proposed approach for generating high-quality modulated signals, making it a suitable tool for component testing at mmW and sub-THz frequencies.

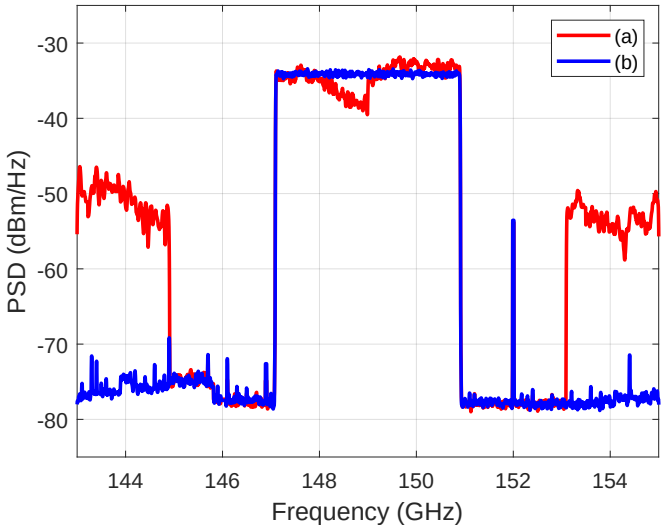


Figure 4.7: Measured PSD at D-band of a 256-QAM 4 GHz bandwidth OFDM signal generated using the proposed method with the PA bypassed: a) before calibration, and b) with the proposed calibration applied.

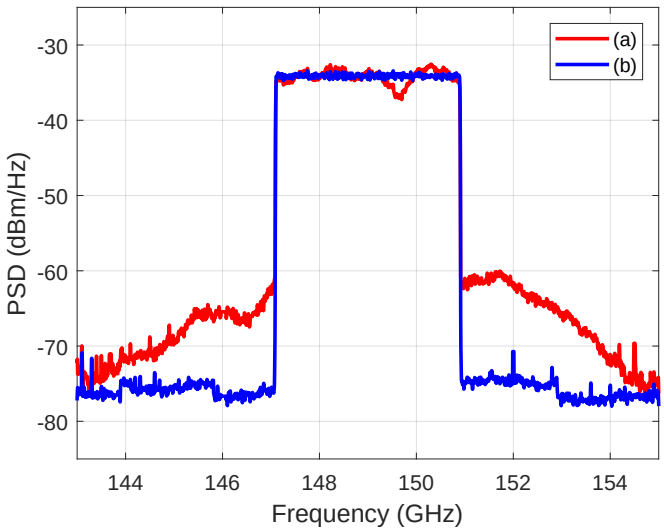


Figure 4.8: Measured PSD at the D-band PA output when driven with a 256-QAM 4 GHz bandwidth OFDM signal: a) before linearization with calibration applied, and b) after linearization with calibration applied.

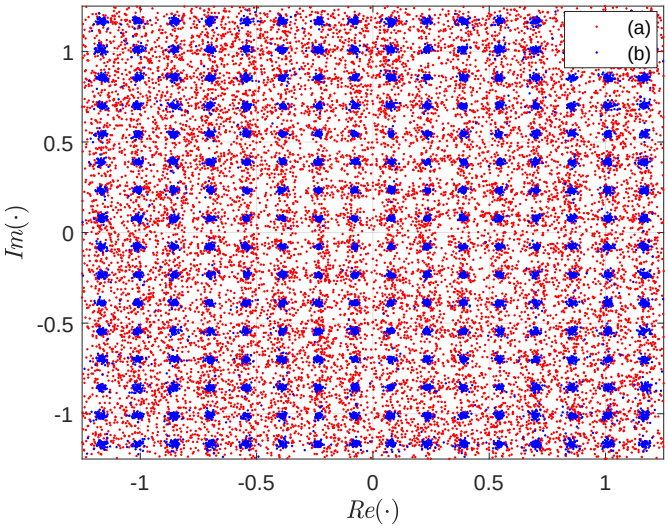


Figure 4.9: Measured constellation at the D-band PA output when driven a 256-QAM 4 GHz bandwidth OFDM signal: a) before linearization with calibration applied, and b) after linearization with calibration applied.

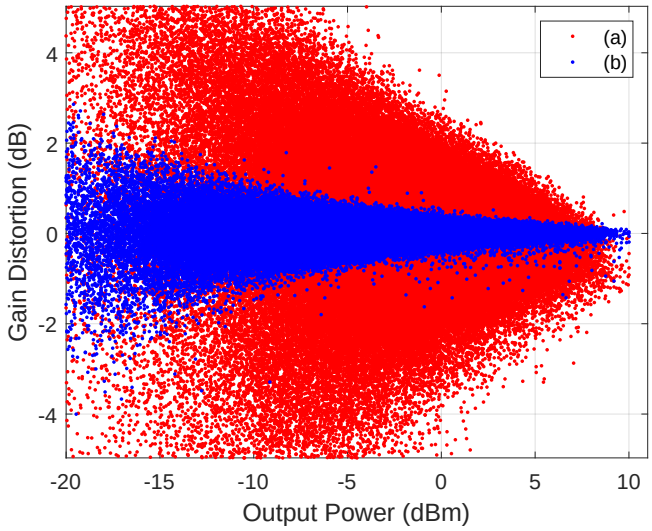


Figure 4.10: Measured gain distortion at the D-band PA output when driven with a 256-QAM 4 GHz bandwidth OFDM signal: a) before linearization with calibration applied, and b) after linearization with calibration applied.

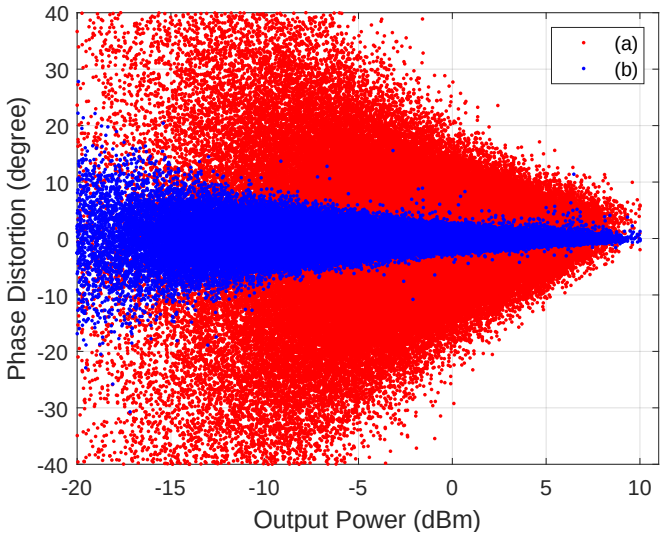


Figure 4.11: Measured phase distortion at the D-band PA output when driven with a 256-QAM 4 GHz bandwidth OFDM signal: a) before linearization with calibration applied, and b) after linearization with calibration applied.

Chapter 5

Comparison Study of IF Combining and RF Combining Architecture for Using Frequency Stitching in Signal Generation

This chapter discusses the contribution from **Publication IV**. This chapter presents a comparison between IF and RF combining architectures, as illustrated in Fig. 5.1.

In the IF combining architecture, sub-band signals are combined at the intermediate frequency (IF) before being upconverted to RF. This approach is inherently limited by the IF bandwidth of the upconverter, which constrains the achievable signal bandwidth.

On the other hand, the RF combining architecture first upconverts each sub-band signal to RF before combining them. This approach allows for wider signal bandwidths. However, it introduces several challenges. One major issue is the requirement for phase-coherent local oscillators (LOs) for the multiple upconverters. Additionally, LO feedthrough can create undesired spurious tones in the RF spectrum, further complicating system design.

Another critical consideration is the performance limitations of the upconverter. Upconverters for mmWave and sub-THz frequencies typically have a low input 1 dB compression point [2, 25]. To avoid driving the upconverter into nonlinearity, the power of the input signal must be limited. This limitation becomes especially problematic when generating wideband signals, as the reduced input power results in thermal noise limited conditions. Consequently, the signal-to-noise ratio (SNR) is reduced, leading to poorer signal quality.

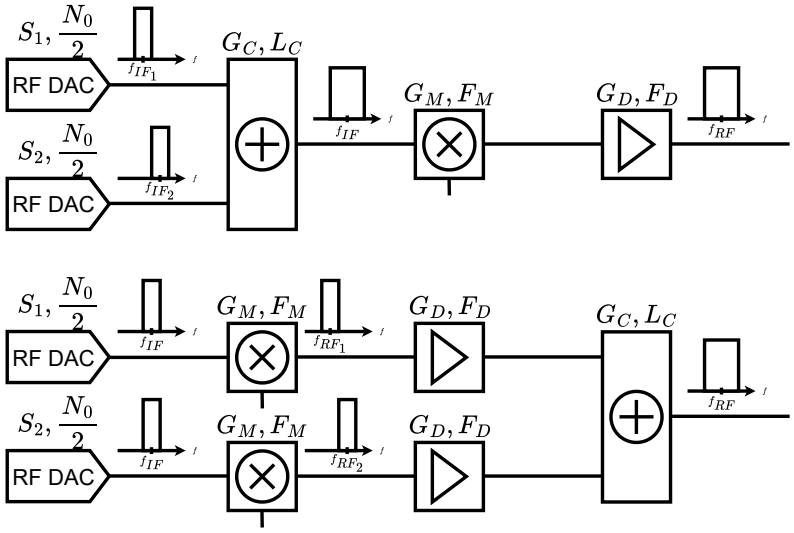


Figure 5.1: Functional block diagram of wideband signal generation at Sub-THz frequencies using frequency bonding, (top) at IF, (bottom) at sub-THz.

This chapter evaluates the performance of the two architectures under two operating conditions: low power, where the upconverter is constrained by thermal noise, and high power, where the upconverter is limited by nonlinear distortion.

5.1 Comparative Analysis of the IF and RF Combining Architectures

This section presents a comparative analysis of the IF and RF combining architectures for wideband signal generation. The analysis will first address the low-power regime, where the up-converter operates in its linear region and the achievable SNR is primarily limited by thermal noise. Subsequently, both architectures are compared in the high-power regime where the up-converter is operated nonlinearly and the achievable SNR is limited by nonlinear distortion.

For simplicity, we will assume a stitching factor of two, utilizing only two DACs.

5.1.1 Noise Limited Analysis

Let S_i (where $i = 1, 2$) represent the generated signal powers from the DACs, each with bandwidth BW. For this analysis, quantization noise will be neglected. Let $N_0/2 = kT_0\text{BW}$ denote the thermal noise power where k is the Boltzmann constant, T_0 is the room temperature in Kelvin taken to equal 293 K. In Fig. 5.1, the IF and RF power combiners are assumed to have perfect port isolation, an insertion loss L_C, and gain G_C defined as $\frac{1}{2L_C}$. The up-converter is characterized by a conversion gain G_M and noise factor F_M. Additionally, the RF driver amplifier is assumed to have a conversion gain G_D and noise factor F_D.

For the IF combining scenario illustrated in Fig. 5.1(top), the SNR at the device under test (DUT) input can be expressed as follows:

$$SNR_{out,IF} = \frac{G_C G_M G_D (S_1 + S_2)}{G_M G_D N_0 + G_D N_{a,M} + N_{a,D}} \tag{5.1}$$

Here, $N_{a,x}$ denotes the added noise by component x and is defined as:

$$N_{a,x} = N_0 G_x (F_x - 1) \tag{5.2}$$

Substituting (5.2) in (5.1) yields:

$$SNR_{out,IF} = \frac{G_C G_M G_D (S_1 + S_2)}{G_D N_0 (G_M F_M + F_D - 1)}. \tag{5.3}$$

For the RF combining case, the SNR at the DUT input is expressed as:

$$SNR_{out,RF} = \frac{G_C G_M G_D (S_1 + S_2)}{\frac{G_M G_D}{L_C} N_0 + \frac{G_D}{L_C} N_{a,M} + \frac{1}{L_C} N_{a,D} + N_{a,C}} \tag{5.4}$$

Substituting (5.2) in (5.4) results in:

$$SNR_{out,RF} = \frac{G_C G_M G_D (S_1 + S_2)}{\frac{N_0}{L_C} (G_M G_D F_M + G_D (F_D - 1) + L_C - 1)} \tag{5.5}$$

Notably, in the special case where $L_C = 1$ (i.e., ideal power combiner), (5.5) simplifies to (5.3). This indicates that both architectures exhibit similar SNR performance when the SNR is noise-limited rather than distortion-limited.

Interestingly, if the RF power combiner in (5.5) is replaced with a duplexer with conversion gain $G_{D'}$ and selectively $S_{D'}$, (5.5) can be re-written as follows:

$$SNR'_{out,RF} = \frac{G_{D'}G_MG_D(S_1+S_2)}{a+b} \tag{5.6}$$

where,

$$a = G_{D'}G_MG_DN_0 + G_{D'}G_DN_{a,M} + G_{D'}N_{a,D} + N_{a,D'}, \tag{5.7}$$

and

$$b = \frac{G_MG_D}{S_{D'}}N_0 + \frac{G_D}{S_{D'}}N_{a,M} + \frac{1}{S_{D'}}N_{a,D}. \tag{5.8}$$

Assuming that $S_{D'} >> 1$, and subtitling (5.2) in (5.6), we obtain:

$$SNR'_{out,RF} \approx \frac{G_MG_D(S_1+S_2)}{N_0(G_DG_MF_M + G_D(F_D-1) + \frac{1}{G_{D'}} - 1)} \tag{5.9}$$

Under the assumption of $G_{D'} = 1$, (5.9) further simplifies to:

$$SNR'_{out,RF} = \frac{G_MG_D(S_1+S_2)}{G_DN_0(G_MF_M + F_D - 1)}. \tag{5.10}$$

From (5.10) we can infer that employing a duplexer instead of a power combiner can provide up to a 3 dB improvement in SNR due to the rejection of out-of-band noise introduced by the mixer and power amplifier. The noise rejection is attributable to the selectivity of the duplexer.

5.1.2 Non-linearity Distortion Limited Analysis

Next, we compare both IF and RF combining architectures in the high-power regime, where the up-converter operates nonlinearly. For simplicity, we assume the RF driver gain is unity. The up-converter can be modeled using in the discrete-time complex baseband equivalent (CBBE) as follows:

$$\tilde{y}[n] = \alpha_1\tilde{x}[n] + \alpha_3\tilde{x}[n]|\tilde{x}[n]|^2 \tag{5.11}$$

where α_1 and α_6 are the model parameters, $\tilde{x}[n]$ is the input signal to the up-converter and $\tilde{y}[n]$ is the output. In the IF combining architecture, the input signal to the up-converter can be expressed as a function of the stitched signals $\bar{x}_1[n]$ and $\bar{x}_2[n]$ as follows:

$$\begin{aligned}\tilde{x}[n] &= \bar{x}_1[n] + \bar{x}_2[n] \\ &= \tilde{x}_1[n]e^{-j\pi\mathrm{BW}} + \tilde{x}_2[n]e^{j\pi\mathrm{BW}}\end{aligned} \tag{5.12}$$

The CBBE DUT input signal can then be expressed as follows:

$$\tilde{y}[n] = \alpha_1(\tilde{x}[n] + \tilde{e}_{IF}[n]) \tag{5.13}$$

where the nonlinear distortion term $\tilde{e}_{IF}[n]$ is given by:

$$\begin{aligned}\tilde{e}_{IF}[n] =& \frac{\alpha_3}{\alpha_1}(\bar{x}_1[n]|\tilde{x}_1[n]|^2 + \bar{x}_2[n]|\tilde{x}_2[n]|^2 + \bar{x}_1^2[n]\bar{x}_2^*[n] \\ &+ 2\bar{x}_2[n]|\tilde{x}_1[n]|^2 + 2\bar{x}_1[n]|\tilde{x}_2[n]|^2 + \bar{x}_2^2[n]\bar{x}_1^*[n])\end{aligned} \tag{5.14}$$

For the RF combining architecture, the input to each up-converter is $\sqrt{2}\bar{x}_i$. The $\sqrt{2}$ is used to ensure that the IF and RF combining architectures deliver the same power to the DUT input. The DUT input $\tilde{y}[n]$ can be expressed as a function of the up-converters outputs $\bar{y}_1[n]$ and $\bar{y}_2[n]$ as follows:

$$\tilde{y}[n] = \frac{1}{\sqrt{2}}(\bar{y}_1[n] + \bar{y}_1[n]) \tag{5.15}$$

Each up-converter output is modeled as:

$$\tilde{y}_i[n] = \sqrt{2}\alpha_1(\bar{x}_i[n] + \bar{e}_{i,RF}[n]) \tag{5.16}$$

Substituting (5.16) in (5.15) we obtain:

$$\tilde{y}[n] = \alpha_1(\tilde{x}[n] + \tilde{e}_{RF}[n]) \tag{5.17}$$

where the nonlinear distortion term $\tilde{e}_{RF}[n]$ is:

$$\begin{aligned}\tilde{e}_{RF}[n] &= \bar{e}_{1,RF}[n] + \bar{e}_{2,RF}[n] \\ &= 2\frac{\alpha_3}{\alpha_1}(\bar{x}_1[n]|\tilde{x}_1[n]|^2 + \bar{x}_2[n]|\tilde{x}_2[n]|^2)\end{aligned} \tag{5.18}$$

Comparing the out-of-band distortion terms in both cases, we observe that in the RF combining case in (5.14) and (5.18), the nonlinear distortion is contained within $4 \times$ BW. In contrast, for the IF combining case, the distortion spreads over a larger bandwidth of $6 \times$ BW. This increase is due to the presence of distortion cross terms i.e., $\bar{x}_2^2[n]\bar{x}_1^*[n]$ and $\bar{x}_1^2[n]\bar{x}_2^*[n]$.

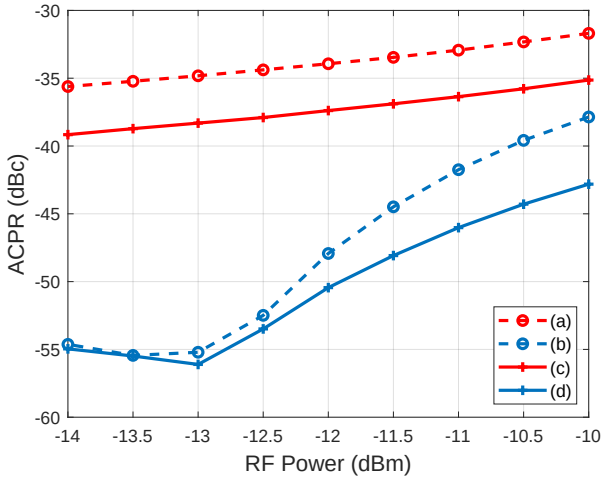


Figure 5.2: Simulated ACPR as a function of power sweep for: (a) IF combining architecture before linearization, (b) after linearization, (c) RF combining architecture before linearization, and (d) after linearization.

5.2 Simulation for the IF and RF Combining Architecture

To assess the impact of these differences on the achievable adjacent-channel power ratio (ACPR), we conducted a simulation comparing the signals generated by both architectures using a nonlinear up-converter. The results, plotted for varying powers at the DUT input both before and after linearization, are presented in Fig. 5.2. The results reveal that the ACPR at the DUT input before linearization for the IF combining architecture (Fig. 5.2 (a)) is approximately 3 dB worse than that of the RF combining architecture (Fig. 5.2 (b)). Furthermore, after applying linearization, the RF combining architecture demonstrates superior linearization performance, as shown in Fig. 5.2 (d), compared to the IF combining architecture in Fig. 5.2 (c).

5.3 Experimental Validation

5.3.1 Measurement Setup

To validate the theoretical analysis presented in the previous section, the measurement setup illustrated in Fig. 5.3 was developed. The signal source for the experiments was a

14-bit, 2 GHz bandwidth, 2.4 Gsps RF arbitrary waveform generator (RF-AWG) (M5300A from Keysight), which provides four synchronous, phase-coherent channels. For the RF combining architecture, two channels of the RF-AWG are connected to two D-band up-converters, followed by a D-band power combiner. In the IF combining architecture, two channels from the RF-AWG are first combined at a low frequency using a power combiner (Marki Microwave PD0140), then routed to a D-band up-converter. Both architectures are then connected to the same receiver chain.

The receiver setup consists of a D-band RF driver amplifier, a D-band bandpass filter, a D-band down-converter, and an IF down-converter (M5201A from Keysight), followed by a digitizer (M5200A from Keysight). The receiver employs a frequency-stitching technique, enabling wideband signal analysis up to 12 GHz. The LO sources for the up/down-converters are generated using two channels of the RF-AWG. For the IF combining transmitter architecture, the RF-AWG provides the same LO source for both the up- and down-converters. In the RF combining architecture, two LO sources are supplied from the RF-AWG to the two up-converters, while the down-converter shares the LO with one of the up-converters. Both transmitter architectures generate signals at 142.5 GHz, and the D-band down-converter in the receiver architecture down-converts them to an IF of 10.5 GHz. The measurement signal used to validate the theory was a 256-QAM, 1.2 GHz orthogonal frequency-division multiplexing (OFDM) signal with subcarrier spacing set to 240 KHz. The linearization scheme used in the reported results is based on the iterative learning control.

5.3.2 Measurement Results

Fig. 5.4 and Fig. 5.5 present, respectively, the measured ACPR and EVM as a function of power sweep for: (a) the IF combining architecture before linearization, (b) after linearization, (c) the RF combining architecture before linearization, and (d) after linearization. At low power and after linearization, both architectures show ACPR values of approximately -55 dBc, as seen in (b) and (d), confirming the theory that both architectures achieve similar SNR performance at lower power levels. However, as power increases and the down-converter enters its nonlinear region, the RF combining architecture outperforms the IF combining architecture, with up to a 8 dB improvement in ACPR. From Fig. 5.5, after linearization, both architectures achieve EVM values as low as 1%, as shown in (b) and (d). However, the RF combining architecture in (d) exhibits slightly higher EVM than the IF combining architecture in (b). This degradation is attributed to the phase noise from the LOs, which affects the quality of the stitched signal at D-band.

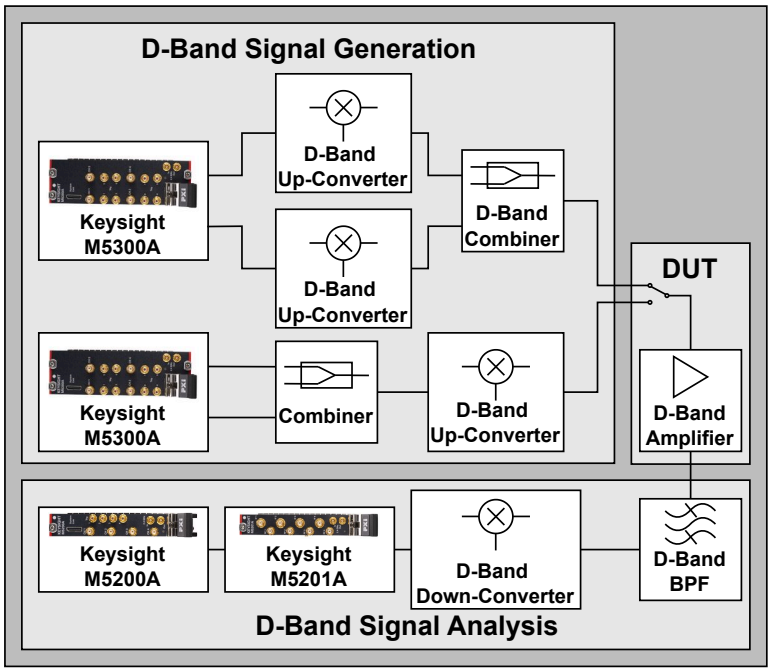


Figure 5.3: Measurement setup.

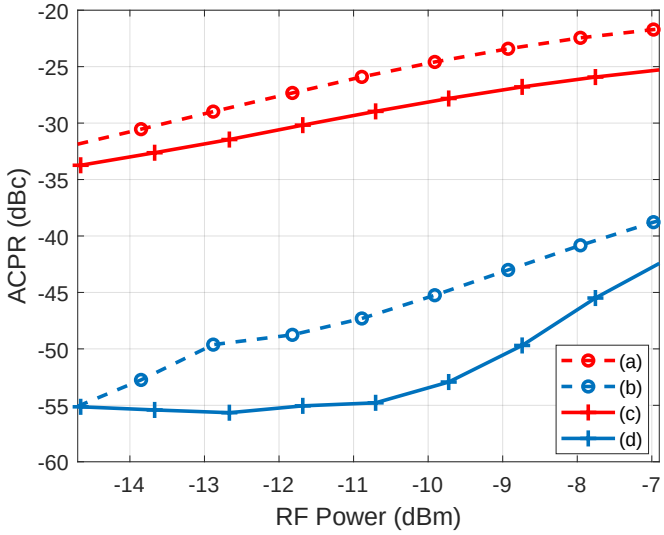


Figure 5.4: Measured ACPR as a function of power sweep for: (a) the IF combining architecture before linearization, (b) after linearization, (c) the RF combining architecture before linearization, and (d) after linearization.

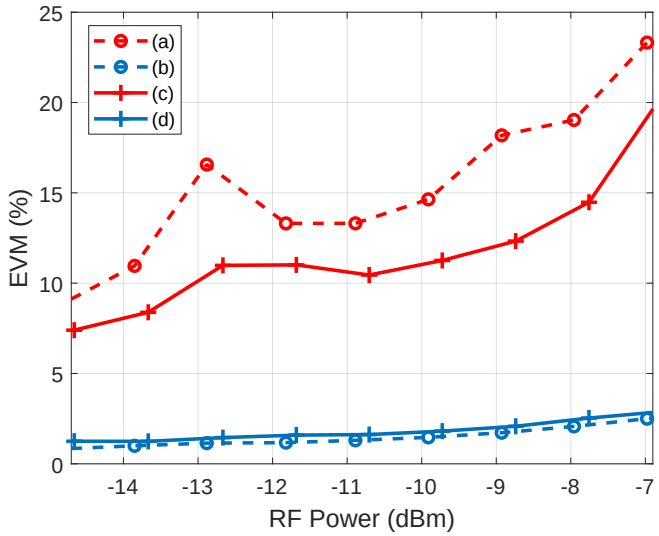


Figure 5.5: Measured EVM as a function of power sweep for: (a) the IF combining architecture before linearization, (b) after linearization, (c) the RF combining architecture before linearization, and (d) after linearization.

Fig. 5.6 illustrates the power spectral density (PSD) of the signal at an RF power of -10 dBm, generated using: (a) the IF combining architecture before linearization, (b) after linearization, (c) the RF combining architecture before linearization, and (d) after linearization. For the IF combining architecture, the ACPR and EVM improved from -25.9 dBc and 13.3% in (a) to -47.3 dBc and 1.3% in (b). Similarly, for the RF combining architecture, the ACPR and EVM improved from -28.9 dBc and 10.5% in (c) to -54.7 dBc and 1.6% in (d). These results confirm that both architectures are suitable for component testing, with the RF combining architecture demonstrating a higher ACPR while maintaining comparable signal quality at higher power levels.

5.4 Conclusion

In this chapter, a comparative analysis is presented for two wideband signal generation architectures for sub-THz frequencies: IF combining and RF combining. The study explores their performance across different power regimes, focusing on signal integrity and dynamic range. In low-power scenarios, where thermal noise is the primary limitation, both architectures deliver similar SNR. However, at higher power levels, where nonlinear distortion becomes dominant, the RF combining architecture outperforms the IF combining

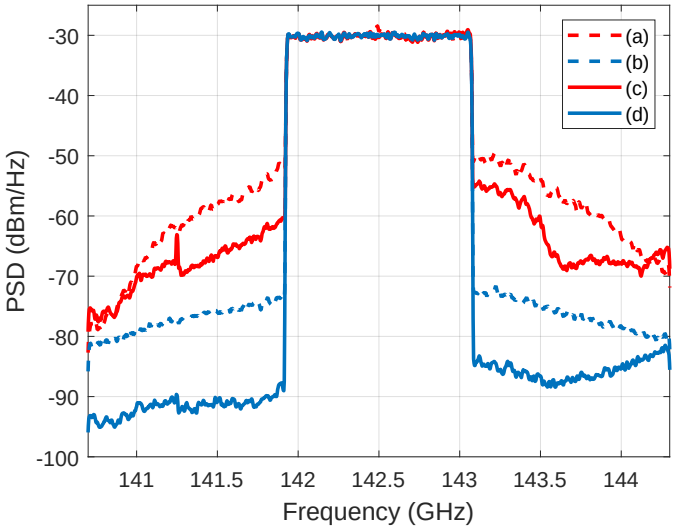


Figure 5.6: Power spectral density of the signal at an RF power of -10 dBm, generated using: (a) the IF combining architecture before linearization, (b) after linearization, (c) the RF combining architecture before linearization, and (d) after linearization.

approach, achieving up to 8 dB improvement in ACPR.

Chapter 6

Conclusion

This thesis has presented solutions for generating wideband signals to meet the demands of 6G wireless communication standards. The research focused on developing and validating frequency-stitching-based wideband signal generation methods, evaluating their performance across different architectures, and addressing the challenges of signal quality and system calibration.

Initially, two wideband signal generation methods were proposed. The first method leverages periodic test signal properties for instrumentation, while the second method utilizes the frequency-domain modulation characteristics of OFDM signals for real-time applications. These methods were validated experimentally at X-band and D-band frequencies, demonstrating excellent signal quality, with EVMs as low as 0.3% for a 7.2 GHz 256-QAM OFDM signal and supporting modulation bandwidths up to 8 GHz.

A comparative study highlighted the advantages of the proposed methods over existing signal generation techniques. Specifically, the proposed frequency-stitching method and an IQ DAC with IQ mixer architecture outperformed a high-speed DAC approach in component testing, achieving superior ACPR of -60.9/-63.8 dBc and -58.4/-62.4 dBc, respectively, compared to -45.8/-49.1 dBc for the high-speed DAC method.

Subsequently, the proposed methods were applied to an IQ DAC and IQ mixer architecture to achieve even higher bandwidths. A novel calibration technique was developed to address IQ imbalances and inter-channel distortions. This technique employed non-uniform interleaved tones to calibrate all signal paths simultaneously, ensuring phase and amplitude alignment. Experimental validation at D-band (around 149 GHz) demonstrated the successful generation of 256-QAM OFDM signals with an instantaneous bandwidth of 12 GHz and a peak data rate of 96 Gbps. The calibration technique significantly improved

EVM and NMSE from 82.6% and 23.8% to less than 2% and 1%, respectively. Additionally, the approach was used to linearize a D-band power amplifier, improving ACPR from -27.8/-26 dBc to -42.8/-43.1 dBc and reducing EVM from 8.5% to 1.2%, while maintaining a linearization bandwidth of 12 GHz.

Finally, a comparative analysis of IF combining and RF combining architectures for wideband signal generation at sub-THz frequencies was conducted. Both architectures demonstrated similar SNR under low-power conditions. However, under high-power scenarios, where nonlinear distortion becomes significant, the RF combining approach exhibited superior performance, achieving up to 8 dB improvement in ACPR compared to the IF combining method.

In conclusion, this research has advanced the state-of-the-art in wideband signal generation for mmWave and sub-THz frequencies, demonstrating practical solutions for high-quality signal generation and calibration. The proposed methods and architectures offer significant potential for 6G wireless communication systems, especially in instrumentation and component testing applications.

6.1 Future Work

This thesis demonstrated two frequency-stitching methods for extending bandwidth in signal generation and validated their performance across various architectures. While the methods produced promising results, several practical considerations remain for further investigation:

6.1.1 DPD for Nonlinearity in Upconverter

Chapter 5 highlights the superior performance of RF combining architectures over IF combining at high power levels, where nonlinearity from the upconverter becomes significant. Unlike PAs, the nonlinearity in upconverters may exhibit different characteristics, potentially requiring tailored linearization techniques. Most existing DPD models are optimized for PA linearization, so future work should explore the effectiveness of these models in addressing upconverter nonlinearity. Developing or adapting DPD algorithms specifically for upconverter nonlinearity could further improve signal quality in RF combining architectures.

6.1.2 DPD for Nonlinearity from Different Sub-Bands

Even if upconverter nonlinearity behaves similarly to PA nonlinearity, challenges remain with the RF combining architecture. Out-of-band distortions arise from sub-bands at the signal edges, and central sub-band distortions can influence adjacent sub-bands. One potential solution is to apply DPD individually to each sub-band path. However, this approach requires significant computational resources and additional hardware to manage the increased processing load. Future work could investigate more efficient methods to address sub-band distortions, such as adaptive or distributed DPD techniques, which balance performance with resource constraints.

Addressing these challenges would enhance the practicality and robustness of frequency-stitching methods for wideband signal generation, further advancing their application in high-frequency wireless systems.

References

[1] IEEE Standard for Information Technology–Telecommunications and Information Exchange between Systems Local and Metropolitan Area Networks–Specific Requirements Part 11: Wireless LAN Medium Access Control (MAC) and Physical Layer (PHY) Specifications Amendment 1: Enhancements for High-Efficiency WLAN. *IEEE Std 802.11ax-2021 (Amendment to IEEE Std 802.11-2020)*, pages 1–767, 2021.

[2] Toshiaki Abe, Shinsuke Hara, Akifumi Kasamatsu, Yohtaro Umeda, and Kyoya Takano. A D-band wideband double-balanced source-driven up-conversion mixer in 40-nm CMOS. In *2023 IEEE Int. Symp. on Radio Freq. Integration Technol. (RFIT)*, pages 73–75, 2023.

[3] Xi Chen, S. Chandrasekhar, Sebastian Randel, Greg Raybon, Andrew Adamiecki, Peter Pupalaikis, and Peter J. Winzer. All-Electronic 100-GHz Bandwidth Digital-to-Analog Converter Generating PAM Signals up to 190 GBaud. *J. Lightw. Technol.*, 35(3):411–417, 2017.

[4] F. Colodro, J. M. Martínez-Heredia, J. L. Mora, J. Ramirez-Angulo, and A. Torralba. Time-Interleaving Sigma–Delta Modulator-Based Digital-to-Analog Converter With Time Multiplexing in the Analog Domain. *IEEE Trans. Circuits Syst. II: Express Briefs*, 70(2):441–445, 2023.

[5] Andreas Czylwik, Stefan Bieder, and Marius Sichma. Extreme wideband arbitrary waveform generator based on frequency multiplexing. In *2017 XXXIInd General Assem. Scientific Symp. Int. Union Radio Sci. (URSI GASS)*, pages 1–4, 2017.

[6] Lucas Duncan, Brian Dupaix, Jamin J. McCue, Brandon Mathieu, Matthew LaRue, Vipul J. Patel, Mesfin Teshome, Myung-Jun Choe, and Waleed Khalil. A 10-bit DC-20-GHz Multiple-Return-to-Zero DAC With ¿48-dB SFDR. *IEEE Journal of Solid-State Circuits*, 52(12):3262–3275, 2017.

[7] Agustín C. Galetto, Benjamín T. Reyes, Damián A. Morero, and Mario R. Hueda. Adaptive Background Compensation of Frequency Interleaved DACs With Application to Coherent Optical Transceivers. *IEEE Access*, 9:41821–41832, 2021.

[8] Daniel Gruber, Martin Clara, Ramon Sanchez, Yu-shan Wang, Christoph Duller, Gerald Rauter, Patrick Torta, and Kamran Azadet. 10.6 A 12b 16GS/s RF-Sampling Capacitive DAC for Multi-Band Soft-Radio Base-Station Applications with On-Chip Transmission-Line Matching Network in 16nm FinFET. In *2021 IEEE International Solid-State Circuits Conference (ISSCC)*, volume 64, pages 174–176, 2021.

[9] Houssam Eddine HAMOUD, Tibault REVEYRAND, Sebastien MONS, and Edouard NGOYA. A Comparative Overview of Digital Predistortion Behavioral Modeling for Multi-standards Applications. In *2018 International Workshop on Integrated Nonlinear Microwave and Millimetre-wave Circuits (INMMIC)*, pages 1–3, 2018.

[10] Garen Hovakimyan, Pirooz Hojabri, Gregory A. Martin, and Patrick Satarzadeh. Digital Correction of Time Interleaved DAC Mismatches. In *2019 IEEE Int. Symp. Circuits Syst. (ISCAS)*, pages 1–5, 2019.

[11] Si-Nai Kim, Woo-Cheol Kim, Min-Jae Seo, and Seung-Tak Ryu. A 65-nm CMOS 6-Bit 20 GS/s Time-Interleaved DAC With Full-Binary Sub-DACs. *IEEE Trans. Circuits Syst. II: Express Briefs*, 65(9):1154–1158, 2018.

[12] Woo-Cheol Kim, Dong-shin Jo, Yi-Ju Roh, Ye-Dam Kim, and Seung-Tak Ryu. A 6b 28GS/s Four-channel Time-interleaved Current-Steering DAC with Background Clock Phase Calibration. In *2019 Symp. VLSI Circuits*, pages C138–C139, 2019.

[13] Christoph Krall, Christian Vogel, and Klaus Witrisal. Time-Interleaved Digital-to-Analog Converters for UWB Signal Generation. In *2007 IEEE Int. Conf. Ultra-Wideband*, pages 366–371, 2007.

[14] Bao Li, Long Zhao, Jiangfeng Wu, and Yuhua Cheng. A 12GS/s 6-bit DAC with 4–2 Segmentation in 40nm CMOS. In *2018 IEEE International Symposium on Circuits and Systems (ISCAS)*, pages 1–5, 2018.

[15] Junpeng Liang, Jia Chai, Xue Chen, Guo-Wei Lu, Zhenhua Feng, Liangjun Zhang, and Weiming Wang. Receiver IQ Imbalance and Skew Compensation for High Order Modulation Formats by Frequency Domain 4 × 2 MIMO. *Journal of Lightwave Technology*, 41(2):558–569, 2023.

[16] Xingqin Lin, Lopamudra Kundu, Chris Dick, Emeka Obiodu, Todd Mostak, and Mike Flaxman. 6G Digital Twin Networks: From Theory to Practice. *IEEE Communications Magazine*, 61(11):72–78, 2023.

[17] Farouk Mkadem, Marie Fares, Slim Boumaiza, and J. Wood. Complexity-reduced Volterra series model for power amplifier digital predistortion. *Analog Integrated Circuits and Signal Processing*, 79, 05 2014.

[18] Prasidh Ramabadran, Sidath Madhuwantha, Pavel Afanasyev, Ronan Farrell, and John Dooley. Wideband Interleaved Vector Modulators for 5G Wireless Communications. In *2018 IEEE MTT-S Int. Micro. Workshop Ser. 5G Hardware Syst. Technol. (IMWS-5G)*, pages 1–3, 2018.

[19] Jaeku Ryu. 4G/LTE - LTE Advanced.

[20] Hirofumi Sasaki, Yasunori Yagi, Riichi Kudo, and Doohwan Lee. 1.58 Tbps OAM Multiplexing Wireless Transmission With Wideband Butler Matrix for Sub-THz Band. *IEEE Journal on Selected Areas in Communications*, 42(6):1613–1625, 2024.

[21] Christian Schmidt, Christoph Kottke, Volker Jungnickel, and Ronald Freund. Enhancing the Bandwidth of DACs by Analog Bandwidth Interleaving. In *Broadband Coverage Germany; 10. ITG-Symp.*, pages 1–8, 2016.

[22] Zi Jun Su, Ahmed Ben Ayed, and Slim Boumaiza. Wideband vector signal generation using multiple narrowband phase-coherent synchronous signal channels. In *2024 103rd ARFTG Microwave Measurement Conference (ARFTG)*, pages 1–4, 2024.

[23] Zi Jun Su, Ahmed Ben Ayed, Nizar Messaoudi, Patrick Mitran, and Slim Boumaiza. Frequency-stitching-based ultrawideband signal generation for 6g component/system testing: Achieving 12-ghz instantaneous bandwidth and 96-gbps data rate at d band. *IEEE Transactions on Microwave Theory and Techniques*, pages 1–10, 2024.

[24] Zi Jun Su, Nizar Messaoudi, Ahmed Ben Ayed, Jean-Pierre Teyssier, and Slim Boumaiza. Comparison of signal generation approaches for component testing at d-band. In *2024 103rd ARFTG Microwave Measurement Conference (ARFTG)*, pages 1–4, 2024.

[25] Dawei Tang, Zekun Li, Peigen Zhou, Sidou Zheng, Jixin Chen, Zhe Chen, Debin Hou, and Wei Hong. A 300 GHz SiGe double-balanced passive third harmonic mixer using PMOS varactors. In *2022 IEEE MTT-S Int. Wireless Symp. (IWS)*, volume 1, pages 1–3, 2022.

[26] Keysight Technologies. M8199A Arbitrary Waveform Generator. Technical report, Keysight Technologies. https://www.keysight.com/us/en/product/M8199A/arbitrary-waveform-generator-128-256-gsas.html.

[27] International Telecommunication Union. Framework and overall objectives of the future development of IMT for 2030 and beyond. Technical report, International Telecommunication Union. https://www.itu.int/rec/R-REC-M.2160-0-202311-I/en.

[28] International Telecommunication Union. IMT Vision - Framework and overall objectives of the future development of IMT for 2020 and beyond. Technical report, International Telecommunication Union. https://www.itu.int/rec/r-rec-m.2083.

[29] M. Valkama, M. Renfors, and V. Koivunen. advanced methods for i/q imbalance compensation in communication receivers. *IEEE Transactions on Signal Processing*.

[30] Chun Wang, Ibrahim Abdo, Chenxin Liu, Carrel da Gomez, Jill Mayeda, Hans Herdian, Wenqian Wang, Xi Fu, Dongwon You, Abanob Shehata, Sunghwan Park, Yun Wang, Jian Pang, Hiroyuki Sakai, Atsushi Shirane, and Kenichi Okada. A Sub-THz Full-Duplex Phased-Array Transceiver With Self-Interference Cancellation and LO Feedthrough Suppression. *IEEE Journal of Solid-State Circuits*, 59(4):978–992, 2024.

[31] Daniel Widmann, Tobias Tannert, Xuan-Quang Du, Thomas Veigel, Markus Grözing, and Manfred Berroth. A Time-Interleaved Digital-to-Analog Converter up to 118 GS/s With Integrated Analog Multiplexer in 28-nm FD-SOI CMOS Technology. *IEEE J. Solid-State Circuits*, 59(3):908–922, 2024.

[32] Hiroto Yamamoto, Atsushi Fukuda, Sumire Aoki, Hiroshi Hamada, Hiroshi Okazaki, and Yasunori Suzuki. Wideband Single Carrier Transmitter Configuration Equalizing Non-flat Frequency Response. In *2022 27th Asia Pacific Conference on Communications (APCC)*, pages 209–213, 2022.

[33] Victor Åberg, Christian Fager, Rui Hou, and Lars Svensson. An 11 GS/s 2×10b 20–26 GHz Modulator using Segmented Non-Linear RF-DACs and Non-Overlapping LO signals. In *2022 IEEE Radio Frequency Integrated Circuits Symposium (RFIC)*, pages 143–146, 2022.